Accepted for publication in *Journal of Geophysical Research*

Small Scale Temperature Variations in the Vicinity of NLC: Experimental and Model Results

M. Rapp, F.-J. Lübken and A. Müllemann
Leibniz Institute of Atmospheric Physics, Kühlungsborn, Germany

G. E. Thomas
Laboratory for Atmospheric and Space Science, University of Colorado, Boulder, CO, USA

E. J. Jensen
NASA Ames Research Center, Moffett Field, CA, USA

Abstract

Gravity waves (GWs) are a ubiquitious dynamical feature of the polar summer mesopause region. During three summer campaigns, in 1991, 1993 and 1994 we launched seven sounding rockets from the North Norwegian island Andøya. Each of these payloads carried an ionization gauge capable of measuring the total atmospheric density at a high spatial resolution. From these measurements, temperature profiles were determined for altitudes between 70 and 110 km, with an altitude resolution of 200 m. The temperature profiles reveal significant rms-variations that are as large as 6 K at 80 km, 10 K at 85 km, and even 20 K at 95 km.

During three out of the seven launches a bright noctilucent cloud (NLC) was simultaneously detected by our ground-based lidar and by rocket-borne in situ experiments. During these flights, the NLC is located close to a local temperature minimum below the mesopause. We then estimated gravity wave parameters from accompanying falling sphere and chaff wind observations and found signatures that the wave periods during the NLC cases were on the order of 7-9 hours, with corresponding horizontal wavelengths of 600-1000 km.

Motivated by these observations, we used a microphysical model of NLC generation and growth to study the interaction between GWs and NLC. Based on recently measured and modeled temperatures and water vapor mixing ratios, and our gravity wave parameter estimates, we find that the NLC layer indeed follows the motion of the cold phase of the wave by means of a complex interplay between ice crystal sedimentation, transport by the vertical wind, and simultaneous growth. It turns out that the history of individual particles significantly influences the observed properties of NLC. Furthermore, we find that GWs with periods longer than 6.5 hours amplify NLC while waves with shorter periods tend to destroy NLC. In addition, we can only find a correlation between local temperature minima and the location of the NLC provided that the wave periods are longer than $\sim$6 hours, which is consistent with our wave parameter estimates.

1. Introduction

Noctilucent clouds (NLC) are a striking optical phenomenon observed in the vicinity of the extremely cold polar summer mesopause region [*Jesse*, 1885]. It is now commonly accepted that NLC are the direct consequence of the light scattering properties of small nanometer-size ice particles. At mean temperatures between ~128 K at the mesopause and 150 K at 82 km [*Lübken*, 1999], the relative water vapor content of a few ppm$_v$ [e.g., *Seele and Hartogh*, 1999] leads to a supersaturated gas phase environment where ice particles can nucleate and grow to visible size. For a review on the physics of NLC and their atmospheric environment, we refer to *Thomas* [1991]. Though the basic physics of cloud formation and growth seems to be well understood, questions still remain, such as those about the details of the thermal structure involved, or the consequence of dynamical features like gravity waves. *Lübken et al.* [1996] analyzed five data sets of simultaneous lidar measurements of NLC and falling sphere temperature measurements, plus three data sets of simultaneous NLC and temperature measurements published in the literature. The only consistent feature they found was that in none of the cases did the temperature inside the NLC layer exceed 154 K. However, *Lübken et al.* [1996] find no any apparent correlation between the mesopause temperature and the occurrence of NLC. The authors noted that the lack of correlation between the conditions at the mesopause and NLC occurrence is not expected from the 'standard growth and sedimentation scenario' [e.g., *Turco et al.*, 1982; *Jensen and Thomas*, 1988; *Jensen et al.*, 1989], where it is assumed that the particles nucleate at the mesopause and then grow and sediment down until they have reached visible size. One problem, however, related to the question of correlation between the thermal structure and the occurrence of NLC is that the falling sphere technique utilized by *Lübken et al.* [1996] has a rather poor altitude resolution of only a few kilometers at mesopause heights [*Schmidlin*, 1991]. Therefore, the technique is not capable of resolving temperature fluctuations induced by, for example, gravity waves with short vertical wavelengths on the order of a few kilometers. Gravity waves, on the other hand, are a ubiquitious phenomenon in the polar summer mesosphere and it is well established that they significantly influence the properties of NLC [*Witt*, 1962].

In the current paper, we investigate the role of gravity wave-induced small scale temperature fluctuations in the vicinity of NLC. We first give a short summary of our observational methods in the next section. In section 3, we present results from three rocket campaigns aimed at studying the polar summer mesopause region. During these campaigns a total of seven sounding rockets carrying ionization gauges were launched to measure the total atmospheric density at a high spatial resolution. Applying a recently developed correction method to account for aerodynamic disturbances of the absolute density measurement and using the assumption of hydrostatic equilibrium, we converted the density profiles to temperature profiles with an altitude resolution of ~ 200 m. Furthermore, we used wind data from falling sphere measurements below ~80 km altitude and chaff winds to estimate the intrinsic frequency and horizontal wavelength of the waves inducing the temperature disturbances. We use these temperature profiles and wind observations to interpret simultaneous lidar and rocket-borne in situ observations of noctilucent clouds, and we try to corroborate our findings with independent results published in the literature.

In section 4, we present model results obtained with a two-dimensional microphysical model of the formation and growth of ice particles in the polar summer mesosphere. We also investigate the influence of gravity waves with different wave parameters on the formation and growth of NLC.

Finally, in section 5, we discuss the impact of our observational and theoretical data on our understanding of NLC and their atmospheric environment.

2. Methods of observation

2.1. Rocketborne ionization gauges

Our group has been using rocket-borne ionization gauges to measure total atmospheric density at high resolution since the 1980s [*Lübken et al.*, 1987]. For a technical description of the gauges, see *Hillert et al.* [1994] and *Giebeler et al.* [1993], respectively. In the past, the prime scientific objective has been the deduction of turbulence parameters like the turbulent energy dissipation rate from small-scale relative density fluctuations [*Lübken*, 1992; *Lübken et al.*, 1993; *Lübken*, 1997b]. However, it is also possible to derive absolute densities if there is an absolute calibration of the gauges in the laboratory, provided that aerodynamical disturbances of the density measurements are adequately corrected for. Over the years, the lack of an appropriate theory for the flow regime below 95 km altitude has prevented the deduction of absolute densities [*Lübken*, 1997a]. Only recently has the combination of a direct calibration of the applied ionization gauges in a wind tunnel and model simulations with Monte Carlo techniques [e.g., *Gumbel*, 2001] opened the way to determining density profiles for all altitudes between 70 and 110 km, with an accuracy of 2% [*Rapp et al.*, 2001]. We have now converted these density profiles to temperature profiles assuming hydrostatic equilibrium[1]. Below 95 km altitude, the temperature error is determined entirely by the error of the density measurement (2%) [*Rapp et al.*, 2001], resulting in an uncertainty of $\sim \pm$ 3 K. The altitude resolution of these temperature profiles is 200 m, small enough to resolve temperature fluctuations introduced by, for example, gravity waves with vertical wavelengths > 1 km.

2.2. Falling sphere and chaff cloud measurements

The falling sphere technique is described extensively in the literature [e.g., *Schmidlin*, 1991]. Basically, a meteorological rocket carrying an inflatable metalized sphere is launched to an apogee of $\approx$ 110 km. The sphere is inflated to 1 m diameter, and then tracked down with a high-precision radar. From the measured trajectory, the first and second derivatives are calculated to determine horizontal winds, densities, and temperatures. The emphasis of this paper will be on wind measurements below ~80 km. *Meyer* [1985] compared wind profiles from the falling sphere and chaff foil techniques and found satisfactory agreement between the two techniques for altitudes below $\sim$ 80 km. The chaff foil technique is described in detail in the literature [e.g., *Widdel*, 1990]. The method of observation is similar to the falling sphere technique. However, instead of an inflatable sphere, small metalized foil pieces are deployed from the meteorological rocket. Since the mass-area ratio of these foil pieces is so small ($\sim$ 3.4 g/m^2 compared to ~200 g/m^2 for the falling sphere) they fall considerably slower and thus can adapt their motion to the background wind. As a result, the analysis of chaff cloud trajectories gives winds with a typical error of $\leq$ 2 m/s at 85 km altitude [*Wu and Widdel*, 1989].

2.3. The Rayleigh lidar

Between 1990 and 1995, a Rayleigh lidar was operated at the Andøya Rocket Range by the Atmospheric Physics group at Bonn University. Technical details and previous results from this lidar are published by *Langer et al.* [1995b, a] and *Nussbaumer et al.* [1996]. From the observed lidar signal, the aerosol content of the mesopause region can be characterized by the backscatter ratio R, i.e.,

$$R = 1 + \frac{\beta_{Aer}}{\beta_{Ray}} \tag{1}$$

where β_{Aer} is the backscatter coefficient due to aerosol particles and β_{Ray} is the backscatter coefficient of the background atmosphere. As can be seen from equation 1, the presence of aerosol particles leads to a backscatter ratio which is larger than unity. The required molecular signal at the altitude of the aerosol layer is taken from falling sphere density measurements. Note that the lidar data set presented in this paper has already been published in *Lübken et al.* [1996]. However, at the time of this publication, the small-scale temperature measurements which are part of the focus of this investigation were not available.

3. Simultaneous measurements of small-scale temperature fluctuations, winds, and NLC altitudes

3.1. Temperature and NLC height measurements

During the NLC-91 campaign (Esrange) in the summer of 1991, the SCALE campaign (Andøya) in 1993, and the ECHO campaign (Andøya) in 1994, we launched a total of seven sounding rockets equipped with either the ionization gauge TOTAL (the acronym indicates that the total number density was to be measured) or the Combined Neutral and Electron detector (CONE). Table 1 gives an overview of the seven launches. All seven flights were successful in that absolute number densities and temperatures could be determined from the measurements. The absolute number densities are presented in *Rapp et al.* [2001] and will not be discussed any further here. The results of the seven temperature measurements are presented in Figure 1. Here we have combined all seven temperature profiles into one plot, where subsequent profiles have been shifted by 30 K. For comparison, a mean temperature profile for August 1 derived from a large number of falling sphere measurements [*Lübken*, 1999] is overlayed on each ionization gauge temperature profile. First of all, it is interesting to note that each of the seven profiles shows significant wave-like

[1] Note that scale analysis of the vertical equation of motion shows that this assumption is appropriate even in the presence of low-frequency gravity waves as discussed in section 3.2.

signatures with vertical wavelengths between 3 km and 7 km. We assume that these local disturbances have been induced by gravity waves, and hereafter we will refer to them as 'gravity wave signatures'. This assumption will be justified when we identify similar wave structures in falling sphere and chaff wind profiles obtained shortly before and/or after the sounding rocket launches (see section 3.2 for more details).

To derive a measure of the mean gravity wave activity, we also determined the mean of our temperature profiles and the corresponding rms-variations. The results are presented in Figure 2. The rms-variation is indicated to the left of the profiles every five kilometers. Below 80 km the rms-variation is $\sim$ 5 K. Between 80 km and the mesopause at 88 km, the rms-variation is $\sim$ 5-10 K. Above the mesopause, in the thermosphere, the variations become as large as 20 K. Note that the absence of any variation at 110 km is due to our method of hydrostatic downward integration, which requires the 'guess' of an initial temperature value at the maximum altitude.

Each of the seven temperature profiles reveals at least two local temperature minima between 80 km and 90 km, i.e., the altitude range where NLC are frequently observed. The actual altitudes of the temperature minima, the corresponding temperature values, and the dominant wavelength determined from a Fourier analysis of the temperature fluctuations are summarized in Table 2.

During the SCALE campaign in 1993 and the ECHO campaign in 1994, the Rayleigh lidar of Bonn University was used to measure NLC. For details on the measurements during these campaigns, see *Lübken et al.* [1996]. During two of the five flights during SCALE and ECHO, flight SCT03 and flight ECT07, the lidar detected bright NLC layers overhead of the Andøya Rocket Range. The combined results from the rocket flights and the lidar measurements are presented in Figure 3.

The two simultaneous measurements of NLC altitude and small-scale temperature structure reveal an interesting common feature: during both flights the observed NLC layer is located slightly below a local temperature minimum. Note that, at least for flight SCT03, this coincidence is definitely not due to the horizontal distance of 70 km between the sounding rocket and the lidar measuring volume; the thick horizontal line in Figure 3 indicates the peak of the NLC layer as detected by the onboard broadband photometer 'SLIPS' [*Wilhelm and Witt*, 1989; *Lübken et al.*, 1995]. Unfortunately, we cannot present experimental proof like this for flight ECT07. However, in section 3.2 we estimate that the gravity wave which introduced the local temperature variation during flight ECT07 had a horizontal wavelength on the order of 1000 km. Compared to this rather large wavelength, we can assume the thermal structure to be constant on a scale of 70 km.

We now come to the results from the NLC-91 campaign. Unfortunately, a lidar was not available during this campaign. However, 15 s after the launch of sounding rocket NAT13, a second sounding rocket, designated NAD14, was launched which carried both the broadband photometer 'SLIPS' as well as the particle impact detector 'PAT' [*Wälchli et al.*, 1993]. On the downleg part of the NAD14 flight, the two instruments detected an NLC layer between 83 and 84 km. In Figure 4, we have plotted the temperature profile measured with the TOTAL ionization gauge during flight NAT13 and the altitude range of the NLC layer detected by the SLIPS and PAT sensor during flight NAD14 [*Wälchli et al.*, 1993]. During flight NAT13, the local temperature minimum is located at 84.7 km, $\sim$1.5 km higher than during flights SCT03 and ECT07. The minimum is also less pronounced compared to the other flights. Again, we find that the NLC layer is located slightly below the local temperature minimum.

During the remaining four sounding rocket flights, the absence of NLC was confirmed by either the lidar (SCT06, ECT02, ECT12) [*Lübken et al.*, 1996, their Table 1] or by ground based observers located south of Kiruna (NBT05) [*Goldberg et al.*, 1993]. We note that for some of these flights (SCT06, ECT02), the temperature of the lowermost local minimum was significantly colder ($\sim$ 110 K) than during the flights where an NLC layer was observed. We will discuss this point in detail in section 5.

Summarizing the observations presented in this subsection, we stress the following points: During all seven sounding rocket flights, the highly resolved temperature profiles reveal significant gravity wave disturbances with typical wave amplitudes of $\pm$ 5-10 K in the NLC region. During three of these seven flights an NLC layer was detected by the Rayleigh lidar at the Andøya Rocket Range (SCT03, ECT07) and/or by rocket-borne instruments (SCT03, NAT13). During all three of these flights, the NLC layer was located slightly below a local temperature minimum.

3.2. Estimate of gravity wave parameters from wind observations

All ionization gauge temperature soundings presented in the preceding section were accompanied by falling sphere or chaff wind measurements shortly before and/or after the sounding rocket flight. In order to characterize the gravity waves which introduced the small-scale temperature variations, we estimated intrinsic wave periods by means of a hodograph analysis of the wave perturbations of the zonal and meridional wind profiles assuming the presence of monochromatic gravity waves.

It must be stressed that this assumption is important to the validity of the following analysis; *Eckermann and Hocking* [1989] pointed out that a superposition of linearly polarized small-scale waves - analyzed with the hodograph technique under the assumption of a single monochromatic wave - can lead to period estimates which are statistical artifacts and not geophysical. To avoid this potential error source, it is preferable to analyze the data in the Fourier domain, which allows separate consideration of different wave bands. According to *Eckermann* [1996], this is best done by application of the spectral Stokes parameter method. However, this method requires resolution of the data both in altitude and time in order to derive statistically reliable results [*Eckermann and Vincent*, 1989]. Unfortunately, only single vertical profiles of the winds were available to us, so this method is not applicable to our data. On the other hand, *Vincent et al.* [1996] noted that the hodograph analysis of a superposition of waves with more influence from inertial scale waves should indeed result in a determination of the correct wave parameters. We thus proceed with the hodograph analysis without the explicit proof of the presence of a single monochromatic wave, although we certainly need to crosscheck our results for plausibility, such as whether the wave could have propagated up into the mesopause region.

In the left panel of Figure 5 are the wind measurements from falling sphere flight SCS04. Both the zonal and the meridional wind components show distinct wave disturbances, u' and v', on top of the background winds, u and v, indicated by the dotted lines. The background wind components were determined by fitting the measurements with a second-order polynomial. In the right panel of this figure, we show the hodograph, i.e. $v'(u')$, for altitudes between 75 and 82 km, along with the background wind vector at 82 km altitude. This hodograph shows a prominent elliptic shape. The perturbation wind vector rotates clockwise with increasing altitude, indicating upward energy transport and downward phase propagation in the Northern hemisphere [e.g., *Cot and Barat*, 1986]. From the hodograph, the intrinsic wave period can be deduced by applying the polarization relation, which can be written as [*Hines*, 1989, equation 26 setting $R=f/\omega_{wrong}$]:

$$R = \frac{f}{\omega} + \frac{1}{N}\frac{dv_T}{dz} \tag{2}$$

where R is the axial ratio of the minor to the major axis of the polarization ellipse, f is the Coriolis parameter, ω is the intrinsic wave frequency, N is the Brunt-Väisälä frequency, and v_T is the mean wind velocity component transverse to the direction of wave propagation. Thus, equation 2 explicitly takes into account the transverse shear effect first studied by *Hines* [1989], who found that a strong wind shear could create an elliptical hodograph even for a linearly polarized small-scale wave. In the case of our measurements, $\frac{dv_T}{dz}$ is determined from the background wind profile and the direction of wave propagation that is parallel to the the major axis of the polarization ellipse [e.g., *Cot and Barat*, 1986]. For example, in the case of flight SCS04 the transverse wind shear is 1.5 m/s/km in the altitude range of the hodograph, and from our temperature measurement during flight SCT03, we determine N=0.017 1/s. Together, these yield $\frac{1}{N}\frac{dv_T}{dz} = 0.08$. Comparing this to a total axial ratio of R=0.7, determined from the best fit ellipse to the hodograph, indicates that the wind shear contributes only $\sim$11 % of the total R. With $f=1.37\cdot10^{-4}$ 1/s (for the location of Andøya), equation 2 yields a period of $T=\frac{2\pi}{\omega}$=470 min.

Taking the vertical wavelength from the temperature measurements (see Table 2), the horizontal wavelength is estimated from the dispersion relation of internal gravity waves [e.g., *Gill*, 1982] which can be written as:

$$\omega^2 = \frac{N^2 k_x^2 + F^2 k_z^2}{k_x^2 + k_z^2} \tag{3}$$

Here, $k_x = 2\pi/\lambda_x$ is the horizontal, and $k_z = 2\pi/\lambda_z$ is the vertical wavenumber of the wave. The resulting gravity wave parameters for all available falling sphere and chaff measurements are presented in Table 3.

Note that we only derived gravity wave parameters from falling sphere winds when the hodographs showed an elliptic form. We also included results from two chaff flights, NBC07 and NAC19, which gave data for altitudes between 80 and 90 km. The deduction of horizontal winds from the chaff or foil cloud technique is much more accurate than from falling spheres due to the improved altitude resolution (200 m compared to several kilometers) introduced by the significantly slower fall speed. Unfortunately, only flights NBS01, NBS06 and NBC07, as well as ECS06 and ECS08, were launched close enough together (in time) such that we can compare the wave parameters derived from these consecutive flights to each other. While NBS01 and NBS06, and also ECS06 and ECS08, give very similar results, with period deviations of less than 10 %, chaff flight NBC07 yields a period which is ≈25 % smaller than the falling sphere results from NBS01 and NBS06. Whether this deviation is due to natural variability or the accuracy of the determination of the wave parameters is hard to judge. We estimate that the parameter R can be determined from the hodograph with an accuracy of ∼10 %. This uncertainty mainly arises from the uncertainty in the determination of the background wind fields by fitting the measured wind profiles with a polynomial. Another problem with comparing the falling sphere and chaff winds arises from the differing altitude ranges from which the hodographs were obtained; while the falling spheres only yield reasonable data below ∼80 km, the chaff results are from the 80-90 km range. Thus, we must expect that the observed differences between NBC07 and NBS01 and NBS06 are at least partly geophysical.

In order to check if our wave parameters are reasonable, we also investigated whether wave filtering by the mean horizontal wind allowed for the propagation of the waves to altitudes of 80-90 km. Filtering occurs if $|v_{||} - c|$=0, where $v_{||}$ is the horizontal wind component parallel to the direction of wave propagation and c is the horizontal phase velocity of the wave [*Lindzen*, 1981]. With the falling sphere measurements, we verified that this condition was not satisfied in any of the investigated cases, at least down to altitudes where winds were measured, i.e. down to 30 km. Below 30 km the prevailing wind direction is eastward, with typical windspeeds of 20 m/s [*Fleming et al.*, 1990]. Though our derived phase speeds are of the same order of magnitude, 20-40 m/s, we do not anticipate filtering to be a problem in our particular cases since the waves considered here propagated in the sector between North-East/South-West and North-North-East/South-South-East, such that the projection of the mean flow on the direction of wave propagation never reached a critical value. In addition, it could also be that the waves were not excited in the troposphere, but by the stratospheric jet stream such that they were launched above potentially critical layers of wave filtering.

As a final crosscheck of our gravity wave parameters, we note that at least for flights ECS06/ECS08, the derived wave parameters can be indirectly verified by comparison with the observed apparent 'downward' motion of the NLC layer [*Lübken et al.*, 1996]. *Lübken et al.* pointed out that the observed downward motion of the NLC layer by ∼2 km/h could either be due to the downward phase propagation of a wave or a layer tilt of ∼1 km in the vertical by 100 km in the horizontal. From the wave parameters in Table 2 and 3, we estimate the possible downward motion due to the wave to be $\lambda_z/T \approx$ 8 km/9 h ∼ 0.9 km/h, and the possible tilt to be $\lambda_x/\lambda_z \approx$ 950 km/8 km ∼ 118 km/1 km. Here, it is particularly striking that the tilt estimated from the NLC observations almost perfectly matches the one that we estimate from the derived wave parameters.

3.3. Observations during the CAMP campaign

A literature survey shows that there is only one temperature measurement in the high-latitude summer mesopause region that has an altitude resolution comparable to that of the measurements with the ionization gauges CONE and TOTAL (∼200 m). This measurement was performed during the CAMP campaign from the Swedish launch site Esrange with a so-called 'active falling sphere' on August, 4, 1982 [*Philbrick et al.*, 1984]. The result of this measurement is reproduced in Figure 6. The similarity to the ionization gauge profiles presented in Figure 1 is striking: The vertical wavelength of the observed gravity wave structures is 4-6 km with wave amplitudes between 5 and 10 K. Even more striking is the fact that the NLC layer observed with a photometer during a rocket flight preceding the flight of the active falling sphere by only 27 min showed the maximum optical NLC signal at an altitude of 82.6 km, 900 m below the lowermost temperature minimum shown in Figure 6 (Georg Witt, private communication, 2001). This observed correlation between the local temperature minimum and the NLC height is identical to the results presented in section 3.

4. Model results

In this section, we present results obtained with a microphysical model of noctilucent cloud formation and growth. We first give a short introduction to the microphysical model and then present simulations for a dynamically quiet atmosphere, i.e. without gravity waves. The focus of this section, however, is on the investigation of gravity wave influences on noctilucent clouds. Using gravity wave parameters deduced from our in situ measurements, we investigate whether the observed correlation between gravity-wave induced temperature minima and the altitude of noctilucent clouds occurred by chance due to poor observational statistics, or is the causal consequence of the physical and dynamical environment of the cloud.

4.1. The CARMA model

The **C**ommunity **A**erosol and **R**adiation **M**odel for **A**tmospheres (CARMA) is a further development of a multi-purpose aerosol model described by *Toon et al.* [1988]. Previous versions of CARMA have been used to investigate the physics of noctilucent clouds [*Turco et al.*, 1982; *Jensen and Thomas*, 1988; *Jensen et al.*, 1989]. While these previous studies utilized one-dimensional models, *Jensen and Thomas* [1994] applied a two-dimensional version to the problem of gravity wave effects on NLC. Since the time of this investigation, new data and models, mainly having to do with the water vapor abundance in the polar summer mesosphere [e.g., *Seele and Hartogh*, 1999; *Pumphrey et al.*, 1998; *Englert et al.*, 2000; *Körner and Sonnemann*, 2001], as well as new temperature measurements [*Lübken*, 1999], have become available. In particular, the new data on water vapor suggest significantly higher values than used in the former studies. For example, *Jensen and Thomas* [1994] used a profile with approximately 1 ppm_v at 85 km, whereas the microwave results from *Seele and Hartogh* [1999] suggest higher values of $\sim$2.5 ppm_v at this altitude. The recent three-dimensional model results from *Körner and Sonnemann* [2001] even suggest 3 ppm_v at 85 km. Furthermore, *Jensen and Thomas* [1994] did not have the information about the gravity wave parameters that we present in section 3.2, and thus performed more general and idealized investigations of the influence of gravity waves on NLC. Thus, we conclude that, in order to explain the particular data set presented in this paper, it is a worthwhile exercise to repeat model simulations similar to those done previously using the latest data on water vapor and temperatures.

Just like the previous versions, the CARMA model treats three completely interactive constituents: meteoric smoke particles, ice particles, and mesospheric water vapor. The height profile and the size distribution of meteoric smoke particles are calculated as described in *Hunten et al.* [1980]. For the ice particles, microphysical processes like nucleation and condensational growth are treated, as well as particle sedimentation and transport. Water vapor is diminished by condensation, enhanced by evaporation of ice particles, and transported by horizontal and vertical motion. Above 85 km, water vapor is effectively photodissociated by the energetic Ly-α and Schumann-Runge radiation. For a detailed description of the particular microphysical processes we refer to *Turco et al.* [1982]. Optical signatures of simulated ice particles were calculated using the Mie scattering code described by *Ackermann and Toon* [1981].

4.2. Non-gravity wave reference simulations

We now present model results of NLC simulations for the case of an undisturbed background atmosphere. These results are important as a reference case for the gravity wave simulations we discuss in the next section.

As mentioned before, we used the latest available data set for temperatures, water vapor and the background vertical wind. Temperatures are taken from the recent compilation of falling sphere measurements by *Lübken* [1999] for the first week of July. In this period, temperatures at the mesopause reach the lowest values of the entire season, as low as 129 K. Note that the profile we are using is the average of 25 individual rocket soundings and thus represents the mean atmospheric state for typical summer conditions. The water vapor profile has been adopted from the recent three-dimensional model results from *Körner and Sonnemann* [2001] showing water vapor mixing ratios of 6, 5, and 2 ppm_v at 70, 80, and 90 km altitude, respectively. Finally, the vertical wind profile with a maximum upward wind of 2.5 cm/s at 87 km altitude has been adopted from model simulations with the COMMA/IAP model [*Berger and von Zahn*, 1999]. The photodissociation rate of water vapor by Ly-α and Schumann-Runge radiation has been parameterized as described in *Jensen* [1989]. Note that the profiles of water vapor, vertical wind and photodissociation are internally consistent, i.e. the water vapor profile is in steady state between upward transport and destruction by solar UV-radiation. Calculations were performed for a two-dimensional computational domain with 120 vertical levels between 70 and 100 km altitude, and 40 levels in the horizontal with a grid spacing of 12.5 km. Ice and dust particles were calculated on a radius grid comprising 25 size bins. The smallest and largest sizes were 2 nm and

86 nm for the ice particles and 0.25 nm and 10 nm for the dust particles, respectively. The mass ratio between successive bins was chosen as 1.6, resulting in a very fine grid for small radii which becomes coarser towards larger radii. Note that our maximum ice radius limit of 86 nm does not influence the final results since only a very small number of particles exceed this size. A test run with 40 radius size bins resulted in exactly the same results for the simulated NLC properties. The time step that we applied was 50 s.

In Figure 7, we present the results for the reference model run at one particular horizontal location. In Figure 7a to 7f, we show the temporal evolution of temperature, ice mass, water vapor mixing ratio, saturation ratio, total ice number density, and mean ice radius as a function of altitude. On each of these fields, we have also plotted contour lines of the backscatter ratio that would be measured by a lidar with a wavelength of 532 nm. The evolution of the mass of the ice particles (Figure 7b) as well as the evolution of the total ice number density (Figure 7e) shows that the majority of the ice particles nucleate at altitudes between 86 and 88 km. This altitude range is close to the mesopause, at 88 km, and thus the region of largest saturation (Figure 7d). Nucleation mainly occurs during a short time interval right at the beginning of the simulation. Afterwards, the saturation and amount of available condensation nuclei has been efficiently reduced such that further nucleation is inhibited. Note that our results are not affected by our choice of using the cold July temperatures as the initial condition of the simulation; sensitivity studies in which we slowly lower the temperature profile from 'standard winter' values down to our summer temperature profile do not yield any significant differences. This is mainly because the nucleation rate depends exponentially on temperature. Mesopause temperatures on the order of $\sim$130 K are what is really needed for substantial nucleation to take place.

Our calculations show ice number densities of $\leq$ 600 /cm^3. This is a rather low value compared to estimates of ice number densities based on the analysis of electron biteouts in the vicinity of PMSE [e.g., *Lübken et al.*, 1998] which yield $\sim$ 3000/cm^3 in layers of $\sim$ 1 km thickness. We note that our model produces larger ice number densities if we enhance the number of available condensation nuclei. However, lacking any better knowledge about the altitude profile (and type) of condensation nuclei than that proposed by *Hunten et al.* [1980], we do not speculate on this particular point, but we keep in mind that the low number densities might be an indication of some sort of missing physics in the current model formulation. A detailed investigation of the nucleation mechanism is far beyond the scope of this work, and will be dealt with in a future paper.

After nucleation, the particles sediment due to gravity and the ice mass increases mainly due to the increase of particle radius by condensational growth (Figure 7f). The growth of the ice particles leads to a backscatter ratio of 1.1, which is 0.1 above the Rayleigh background, after $\sim$3.5 hours and a value of 5 after 8 hours. After approximately 16 hours, the height of maximum backscatter signature has come down to $\sim$ 81 km and does not change significantly afterwards. The peak backscatter is mainly determined by the available water vapor amount shown in Figure 7c. During the first 16 hours after nucleation, the water vapor supply in the atmosphere is sufficiently large to allow the ice particles to grow. After that, however, the atmospheric water vapor has been depleted by the freeze drying of the ice particles between 88 and 83 km altitude. After this time, the cloud brightness is controlled by sedimentation and evaporation of the ice particles, as well as the upward transport of water vapor by the mean background wind. It is interesting to note that after 16 hours, the maximum backscatter signal coincides with the altitude region of evaporation. This is evident in Figure 7c, where we can identify a water vapor maximum of $\sim$9 ppm$_v$ at 81.5 km altitude, where we also get a maximum backscatter ratio of $\sim$ 10. We note that the existence of a water vapor maximum at altitudes around 82 km has recently been reported by *Englert et al.* [2000]. A detailed comparison between observations and model calculations of the water vapor redistribution by NLC employing the CARMA model is expected to be published soon [*Stevens et al.*, 2001]. Given the vertical wind of $\sim$2 cm/s, it then takes approximately 2.5 days to transport the water vapor up again to altitudes of $\sim$86 km where a new nucleation cycle can start (not shown here).

Note that the temporal evolution of the cloud shown in Figure 7 is mainly determined by the interplay of growth and sedimentation of the particles. To show this point more clearly, we calculated the trajectories of 40 test particles through the atmospheric fields of temperature, wind, and water vapor (Figure 7). For these trajectory calculations, any horizontal transport is neglected since any change in the most relevant atmospheric background quantities like temperature and water vapor is mainly vertical. Initially, the test particles are equally distributed between 90 and 84 km altitude, the altitudes at which particles nucleate. The trajectories are calculated from:

$$z(t) = z_0 - \int_0^t (w_{sedi}(z(t^{'}), r(t^{'}), t^{'}) - w(z(t^{'}), t^{'}))dt^{'} \quad (4)$$

Here, w_{sedi} is the sedimentation speed as given in *Turco et al.* [1982] and w is the vertical wind; w_{sedi} is a function of both the radius of the particle and altitude because it depends on atmospheric density. The radius of the particle is calculated from:

$$r(t) = r_0 + \int_0^t dr/dt^{'} dt^{'}, \; r_0 = r(t=0) \quad (5)$$

where r_0 is the initial particle radius at t=0 and dr/dt is the particle growth rate as formulated by *Hesstvedt* [1961]. In Figure 8 we show the results of these test particle trajectory calculations. In Figure 8a we show the actual trajectories plotted on top of the vertical wind field, which does not change in time in the absence of a wave. Each particle trajectory has been plotted with a different color in order to mark the identity of the different test particles. In Figure 8b we show the radii of the particles as a function of time. In Figure 8c we present an estimate of the optical signature of the test particles, and in Figure 8d we show the contribution of each particle to this optical signature along their trajectories. The optical signature is found by projecting the particles on an altitude-time grid and then calculating $\sum_i N_i \cdot r_i^6$ where N_i is a weighting factor of the particle trajectory which we take as the number density shown in Figure 7e after $\sim$ 0.5 hours. The summation is over all particles that are located at the corresponding altitude-time grid point. Comparing this scatter signature with the backscatter ratio calculated with the full CARMA model shown in Figure 7, we see that the qualitative behaviour of both quantities is identical. The maximum scatter signal first sediments down to 82 km, and then reaches a steady state after $\sim$ 16 hours. This demonstrates that the main features of the simulated NLC are indeed controlled by a pure growth and sedimentation process. In Chart b of Figure 8, we see that the initial increase of the scatter signal is caused by the radius growth and sedimentation of the particles which started between 84 and 85 km (orange to red trajectories). After 10-12 hours, these particles have reached their maximum radii of 60-70 nm. As they began in an altitude region of moderate supersaturation (Figure 7d), only a few particles nucleated (Figure 7e) and thus did not have to compete with other particles for the available amount of water vapor. However, upon sinking below an altitude where S is larger than unity (indicated by the thick black line in Figure 8c) the particles quickly evaporate. Particles coming from higher altitudes do experience the competition for water vapor (see Figure 7c, after 12 hours at 87 km) such that they grow more slowly and thus also sediment more slowly. Finally, we emphasize that a considerable part of the cloud exists at altitudes where S<1.

We conclude that the entire development of the simulated NLC is explained by a growth and sedimentation mechanism. In the next section we investigate whether this conclusion still holds when temperature and water vapor are disturbed by the influence of gravity waves and if we can explain the observed coincidence of local temperature minima and maximum brightness of the NLC.

4.3. Gravity wave simulations

4.3.1. Simulations for observed wave parameters. We performed model simulations for gravity wave parameters obtained from the results of the ionization gauge flight SCT03 (wave period=470 min, horizontal wavelength=595 km and vertical wavelength=6 km). We define gravity wave-disturbed winds, which introduce temperature and density disturbances due to the adiabatic cooling/heating of vertically advected air parcels. Note that we use the same background temperature profile as in the reference case in order to make the different model results comparable. Following *Jensen and Thomas* [1994], the horizontal and vertical wind profiles, u and w, are defined as follows:

$$u = -\tilde{w_0} \cdot \frac{k_z}{k_x} \cdot cos(k_x x + k_z z - \omega t) \quad (6)$$

$$w = \bar{w} + \tilde{w_0} \cdot cos(k_x x + k_z z - \omega t) \quad (7)$$

where $\tilde{w_0} = \frac{\Delta T}{T_0(70km)} \cdot \frac{g\omega}{N^2} \cdot \exp(\frac{z-70km}{2 \cdot 7\ km})$. Above altitudes of 92 km, $\tilde{w_0}$ is additionally multiplied by a factor $\exp(-\frac{(z-92km)^2}{(2 \cdot 5km)^2})$ in order to avoid unreasonably large GW amplitudes. Note that k_z must be negative for downward phase propagation; $\bar{w}$ is the vertical background wind; ΔT=2 K; $T_0(70km)$ is the undisturbed background temperature at 70 km altitude. For comparison with the measured GW amplitudes, we present model temperature disturbances calculated from the above equations together with the measured disturbances from flight SCT03 in Figure 9. The modeled temperature fluctuations match the observations well between the altitudes of 80-90 km where ice particle growth occurs. Above 92 km, measured temperature fluctuations are much larger than the modeled values. The modeled values have been chosen so as not to exceed ~11 K in order to avoid numerical problems close to the boundaries of the model domain which require zero amplitudes. However, we do not anticipate any impact on our model results since ice particles which dominate the optical properties of NLC originate from altitudes between 85 and 86 km anyway (see Figure 13).

The 40 horizontal grid points of our computational domain now comprise one horizontal wavelength where we further assume periodic boundary conditions for reasons of numerical simplicity. This means that an air parcel which is advected out of the eastern boundary of the computational domain is advected into the domain again from the western boundary.

In Figure 10 we present the results of a one-day simulation with the wave parameters noted above. Note that the wave amplitude was switched on gradually over a period of 12 hours until its final value, $\tilde{w_0}$, was reached in order to avoid initial phasing problems between vertical winds and temperatures, for example. Similar to the reference simulation, the optical signature of the NLC starts to rise above the Rayleigh background after approximately 5 hours. Afterwards, however, the brightness observed at one particular altitude varies significantly with time. The backscatter ratio reaches a first maximum after ~13.5 hours and a second one after 21 hours, which are exactly one wave period apart. Furthermore, from Figure 10d we see that the cloud is closely correlated to the altitude regions where the supersaturated air (S>1) reaches altitudes as low as 82 km, the altitude of maximum cloud brightness. Figure 10e and 10f show that the drastic change in cloud brightness is a consequence of change in particle radius rather than number density: While the mean particle radius changes from 70 nm to ~15 nm, the particle number density changes only slightly. Still, the number density reveals the lifting/lowering of air parcels in the cold/warm phase of the gravity wave.

Note that the observed correlation of the cold phase of the wave with the maximum backscatter ratio is not incidentally created by the choice of a particular horizontal location appropriate for a ground based observation from a lidar observatory: In Figure 11 we present x-z-plots of the gravity wave temperature disturbances overlayed with backscatter ratios for different times (for 9, 10.7, 13, 15,18.3, and 24 hours of simulation time). After 9 hours, when the NLC have just reached a backscatter ratio of 5, the contour lines of constant backscatter ratio are not yet confined to either the cold or the warm phase of the wave. However, as time progresses and the backscatter ratio becomes larger, the maximum backscatter ratios coincide more and more with the cold phase of the wave. After 13 hours, there is almost a one-to-one correlation between the location of the cold phase and the location of enhanced backscatter ratio as observed by in situ measurements presented earlier. Afterwards, the cold phase travels from west to the east (towards longer horizontal distances) and the backscatter ratio closely follows this movement. Note that the motion of the backscatter ratio is not due to a pure transport of the ice particles. The motion of an air parcel in the gravity wave field is approximately along a tilted line in the x-z domain. After one wave period, the air parcel has approximately reached its original location. This means that there is no net transport due to a wave and that the observed correlation is a consequence of a combination of transport, evaporation, and growth of the ice particles. In other words, the time scale of temperature change of the wave is such that the microphysical processes (evaporation and growth) happen approximately synchronously. This becomes evident if we compare the results from Figure 11 with results calculated for the case of a gravity wave with a considerably smaller wave period of one hour. Corresponding x-z-plots are presented in Figure 12. Here, it is evident that the time scale of the microphysical processes is considerably longer than that of transport, such that the altitude variation of the backscatter ratio mainly corresponds to the lifting and settling of the air parcels. In section 4.3.2 we will come back to the issue of the time constant of the microphysical system towards changes of the atmospheric environment. We will discuss whether and under what circumstances gravity waves amplify or destroy NLC, and for which wave periods a close correlation between local temperature minima and the location of NLC is to be expected.

In order to infer the relevant physical process leading to the observed correlation of local temperature minima and the backscatter ratio, we performed another test particle simulation, this time in the presence of a gravity wave with a period of 500 min. The results of this simulation are presented in Figure 13. First of all, it is evident from this figure that the periodic vertical wind of the wave has a significant influence on the particle trajectories: The wind field ‘bundles' the particles into three bunches aligned with the downward phase of the wave. Among these particles, the lowermost particles within each bunch reach the largest size, and hence lead to the largest backscatter ratio. Because temperature and vertical wind are out of phase by 90°, the largest particles within each bunch coincide with the minimum temperature value. In addition, Chart b and d of Figure 13 show that some of the particles have 'optimized' their trajectories, in that they reach their maximum size during the second (upward) phase of the vertical wind. The yellow particle which reaches the maximum radius of $\sim$ 85 nm after 17.5 hours already belongs to the first bunch after $\sim$7 hours of downward transport, but is still at such a high altitude in the subsequent upward phase of the wave that it remains in the supersaturated altitude region and can gain additional size for an additional upward and downward phase cycle of the wave. Most interestingly, this 'optimization' of the trajectory finally leads to a larger particle size, and hence larger scattering signal compared to the case when no wave is present (see Figure 8). We will come back to this issue in section 4.3.2.

To summarize, we state that the observed correlation of the local temperature minima with the maximum backscatter is due to a filtering of the particle trajectories by the vertical wind, in combination with the sedimentation of the particles and the optimization of some of the particle trajectories. In this way, the particles are allowed to reside in the supersaturated altitude range for a maximum duration, and thus reach a maximum size which can be even larger than in the non-gravity wave case.

4.3.2. General dependence on wave period. In this subsection we investigate if and for which wave parameters a gravity wave amplifies or destroys NLC. In order to do this, we have performed several gravity wave/NLC simulations with wave periods from 1 hour up to 12 hours. As a measure of the mean brightness of the simulated clouds, we define the 'domain averaged backscatter ratio' DABR:

$$DABR = \frac{\frac{\left(\int_{x(\beta_{Aer}>\beta^*)}\int_{z(\beta_{Aer}>\beta^*)} \beta_{Aer}(x,z)\ dx\ dz\right)}{\left(\int_{x(\beta_{Aer}>\beta^*)}\int_{z(\beta_{Aer}>\beta^*)} dx\ dz\right)}}{\beta_{Ray}(83\ km)} + 1 \quad (8)$$

This means that we first average the backscatter coefficient due to the ice particles in the x-z domain where it supersedes a threshold value of β^* (which we define as the Rayleigh-background at 83 km) and then express it as a backscatter ratio at 83 km.

The results of these model runs are presented in Figure 14. The thick solid line shows the result for the simulation in the absence of a gravity wave, whereas the other lines and symbols show the results for waves with periods from 1 hour to 12 hours. From Figure 14, it appears that waves with periods smaller than 180 min significantly weaken NLC, those with periods from 240 min to 390 min do not strongly influence the NLC brightness, and finally, that waves with periods longer than 420 min at least temporarily amplify NLC. Furthermore, it is important to realize that only in the cases where brightness amplification occurs do we also observe a clear correlation between local temperature minima and the occurrence of NLC. We note that this result, to some extent, supports our earlier results from the gravity wave parameter analysis of falling sphere and chaff winds; in the observed NLC cases we dealt with low frequency gravity waves with periods on the order of 7-9 hours.

This general dependence of NLC brightness on wave periods means that a time scale of approximately 400 min is the fundamental time scale for the growth of the ice particles, at least for the assumed background conditions of the thermal structure, the vertical wind, the water vapor and condensation nuclei. For wave periods larger than this, individual particle trajectories become optimized, in a sense that they can reside for an optimum amount of time in the supersaturated altitude regime and grow to a maximum size. For shorter wave periods, however, the particles are transported downward more rapidly and out of the supersaturated regime such that their growth time is diminished and the NLC brightness is reduced.

5. Discussion

5.1. Comparison with other model results

There are various reports published in the literature which investigate the possible influence of gravity wave-induced temperature disturbances on NLC. For example, *Turco et al.* [1982] used a one-dimensional NLC model to investigate the response of ice particles to a gravity wave with a period of 1.5 hours, a horizontal wavelength of 360 km, a vertical wavelength of 29 km and a temperature amplitude of ±20 K at 85 km. They found that a gravity wave with these characteristics destroys NLC because the ice particles evaporate much quicker in the warm phase of the wave than they grow again in the cold phase. However, we note that this choice of wave parameters was quite arbitrary and not related to any particular observation. Compared to our in situ small-scale temperature measurements which revealed amplitudes on the order of ±5-10 K at 85 km, the amplitudes they selected seem too high.

Jensen and Thomas [1994] took a major step forward by simulating the wave-cloud interaction in a two-dimensional model and also investigating the influence of three idealized wave types - waves with periods of 5 min, 1 hour, and 10 hours. To test the influence of the wave on a 'mature' cloud, they first ran the cloud model into a steady state and then switched on the wave disturbances. All three wave types resulted in a net destruction of the cloud, though their 'case 3 wave', with a period of 10 hours, led to a short amplification before a destruction even more rapid than in the other cases. We note that these results are basically consistent with our results which show that waves with periods less than 6.5 hours tend to weaken or destroy the clouds whereas waves with longer periods amplify the NLC display. However, unlike *Jensen and Thomas* [1994], we have not run the NLC into a steady state first, rather we have gradually switched on the wave disturbance from the very beginning of the simulation. From our test particle calculations we have seen that the brightness amplification observed in our model results was due to the trajectory optimization of a few particles which managed to stay in a supersaturated altitude regime for an optimum amount of time. However, this optimization is impossible if most of the particles have already sedimented to $\sim$ 83 km altitude and are in a steady state between evaporation and upward transport of water vapor. As gravity waves seem to be a ubiquitous phenomenon of the polar mesopause region, it seems questionable whether such an undisturbed 'steady state' of NLC can ever exist. Furthermore, we have used considerably higher water vapor values for the background atmosphere than assumed by *Jensen and Thomas* [1994].

It should also be noted that unlike *Jensen and Thomas* [1994], we ran the model for only 24 hours. We chose such a short simulation time because it is likely that the atmosphere changes significantly over longer periods. In particular, we also neglected horizontal transport due to the meridional wind component. Considering mean meridional winds of $\sim$ 10-15 m/s in the high latitude polar summer mesosphere [*McLandress et al.*, 1996], an ice cloud would be transported 900-1500 km from north to south in one day. Extending the model simulations to longer periods without adjusting the background fields of temperature, water vapor, and vertical wind would probably not yield meaningful results.

The next contribution to the literature with regard to NLC models came from *Klostermeyer* [1998]. He performed a time-scale analysis of the relevant physical processes for the genesis and development of NLC and concluded that if vertical air motions due to tides or gravity waves are considered, then the process of sedimentation is of minor importance and can thus be neglected. Using this model in the simulation of observed tidal structures at NLC altitudes, *Klostermeyer* [2001] demonstrated good agreement between his model results and observations.

However, our test particle trajectory calculations show that the net downward transport of the particles is substantial and significantly contributes to the appearance of NLC, though the vertical velocities of the background wind field do outnumber the sedimentation velocities. As we have shown in section 4.3.1, it is the 'optimization' of particle trajectories through the wind fields in combination with the particle sedimentation which finally lead to our observed correlation of local temperature minima and the occurrence of NLC. In order to confirm this, we ran simulations for which the sedimentation speed was set to zero. In these simulations, the cloud brightness was weak and the cloud occurred near the altitudes where the particles had nucleated, around 86 km. Most important, the correlation between local temperature minima and the maximum backscatter of the particles disappeared. We thus conclude that the sedimentation process of the ice particles is one of the most important processes involved which lead to the observed features of NLC, in particular the correlation of local temperature minima and maximum brightness observed in our in situ experiments.

5.2. Influence of particle history on NLC properties

Our simulations strongly suggest that the history of individual particles and the actual wave parameters are very important in interpreting the optical properties of single NLC observations. However, the stochastic nature of waves leads us to expect that the averaged behavior of NLC over sufficiently long spatial and time scales would reduce, if not eliminate, the sensitivity to the particle histories and wave parameters. For example, it has been proposed that long-term variability of NLC is linked to water vapor changes, due to both solar UV variability [*Garcia*, 1989; *Thomas*, 1995; *Thomas and Olivero*, 2001] and to long-term increases in methane [*Thomas et al.*, 1989]. The influence of decadal-long temperature trends has also been suggested [*Gadsden*, 1990]. An unanswered question is, "What are the scales over which the averaging must take place?" A second question involves whether the waves themselves are subject to long-term changes. It is certainly possible that long-term changes in the underlying winds, which filter the upward propagating waves, could bring about corresponding changes in wave properties.

Note that the history of individual air masses might also be decisive in explaining the absence of NLC, though the thermal structure at the time of observation was favorable. In section 3, we presented temperature data for four rocket flights where the temperature was well below the usually assumed limit of $\sim$ 150 K for the existence of NLC, and still the absence of NLC was confirmed by ground-based observations. At least for flight ECT02, this could be due to the action of a rather short-period gravity wave inhibiting ice particle formation (see section 4.3.2). However, this explanation cannot hold in case of flight NBT05, where wave periods were estimated to be on the order of $\sim$9 hours.

Another possibility is that the temperature inside the air volume under consideration had been too high for ice particle creation for a considerable amount of time. If so, it would take several hours from the time that the temperature starts falling again until a visible cloud is observed. Finally, another possibility could be that we were dealing with 'old' air masses, i.e. those left behind dry by an NLC which evaporated in the meantime. After such an event, it would take at least one day for the mean background wind to transport the water vapor up from 83 km to 86 km, where new particles can nucleate again.

6. Summary

We have presented temperature profiles with a high spatial resolution ($\sim$ 200 m) obtained by rocket-borne ionization gauges in the high latitude summer mesopause region. All of the temperature profiles reveal considerable local temperature disturbances with rms-values as large as 6 K at 80 km, 10 K at 85 km, and even 20 K at 95 km altitude. In three out of seven cases, an NLC was observed by a ground based lidar and/or a rocket-borne detector. In these cases, the NLC was located close to the local temperature minima. In the remaining four cases, no NLC were detected, despite favorable thermal conditions, i.e. temperatures below 150 K. We also used falling sphere winds from below 80 km and chaff foil winds obtained close in time to the temperature soundings, and we estimated gravity wave periods and horizontal wavelengths from a hodograph analysis of the corresponding wind fluctuations where we found signatures that the wave periods during the NLC cases were on the order of 7-9 hours, with corresponding horizontal wavelengths of 600-1000 km.

We then used a microphysical model of mesospheric ice particles in order to simulate the properties of ice clouds in the presence of gravity wave disturbances. For the estimated gravity wave parameters, we can reproduce the observed features of our in situ measurements, i.e. the optical signature of the ice clouds is located close to the local temperature minimum of the wave. In order to identify the physical process leading to this correlation we performed test particle studies through the corresponding atmospheric fields of temperature and vertical wind, and we found that the observed correlation is the consequence of two dominating processes. First, the interplay of the sedimentation of the particles and the background vertical wind bundles the particle trajectories in the downward phase of the wave. This means that the sedimentation process of the particles can by no means be neglected for the overall appearance of a cloud. Second, some particles optimize their paths through the atmospheric fields, reach maximum size, and dominate the optical signature of the ice cloud. Thus, it is the detailed history or trajectory of special particles which controls the optical appearance of a cloud. In other words, this means that the atmospheric conditions, specifically water vapor amount and thermal structure, must be favorable throughout cloud genesis and development, not only at the time of observation. It is important to note that this sets constraints for both the mean atmospheric state (e.g. the thermal structure averaged over the whole period of cloud development) and the short-term variations of water vapor and temperature.

We then performed wave/NLC simulations for periods ranging from 1 hour up to 12 hours. From these simulations, we found that waves with periods less than 400 min tend to destroy NLC whereas waves with longer periods amplify NLC.

Acknowledgments. We are grateful to Georg Witt for providing information about the photometer measurements during the CAMP project and many useful discussions. We have further greatly benefited from the comments of one anonymous reviewer hinting us at potential pitfalls in the hodograph analysis of our wind measurements. M. Rapp and A. Müllemann were supported by the Bundesministerium für Bildung und Forschung under grants 50OE9802 and 50OE9901, respectively. G. E. Thomas was supported by the Aeronomy Program of the National Science Foundation. The rocket flights were supported by the Bundesministerium für Bildung, Wissenschaft, Forschung und Technologie under DARA grant 01OE88027.

References

Ackermann, T. P., and O. B. Toon, Absorption of visible radiation in atmosphere containing mixtures of absorbing and nonabsorbing particles, *Appl. Optics*, *20*, 3661, 1981.

Berger, U., and U. von Zahn, The two-level structure of the mesopause: A model study, *J. Geophys. Res.*, *104*, 22083–22093, 1999.

Cot, C., and J. Barat, Wave-turbulence interaction in the stratosphere: a case study, *J. Geophys. Res.*, *91*, 2749–2756, 1986.

Eckermann, S. D., Hodographic analysis of gravity waves: relationships among stokes parameters, rotary spectra, and cross spectral methods, *J. Geophys. Res.*, *101*, 19169–19174, 1996.

Eckermann, S. D., and W. K. Hocking, Effect of superposition on measurements of atmospheric gravity waves: a cautionary note and some reinterpretaions, *J. Geophys. Res.*, *94*, 6333–6339, 1989.

Eckermann, S. D., and R. A. Vincent, Falling sphere observations of anisotropic gravity wave motions in the upper stratosphere over Australia, *Pure Appl. Geophys.*, *130*, 509–532, 1989.

Englert, C. R., M. H. Stevens, R. R. Conway, M. E.Summers, J. M. R. III, and L. L. Gordley, Oh, h_2o and polar mesospheric clouds: discovery of a double layer h_2o distribution in the polar summer mesosphere, *Eos. Trans. AGU*, *81*, 331, 2000.

Fleming, E. L., S. Chandra, J. J. Barnett, and M. Corney, Zonal mean temperature, pressure, zonal wind, and geopotential height as functions of latitude, *Adv. Space Res.*, *10(12)*, 11–59, 1990.

Gadsden, M., A secular change in noctilucent cloud occurrence, *J. Atmos. Terr. Phys.*, *52*, 247–251, 1990.

Garcia, R. R., Dynamics, radiation and photochemistry in the mesosphere, *J. Geophys. Res.*, *94*, 14,605–14,616, 1989.

Giebeler, J., F.-J. Lübken, and M. Nägele, CONE - a new sensor for in-situ observations of neutral and plasma density fluctuations, *Proceedings of the 11th ESA Symposium on European Rocket and Balloon Programmes and Related Research, Montreux, Switzerland (ESA SP)*, *ESA-SP-355*, 311 – 318, 1993.

Gill, A. E., *Atmosphere Ocean dynamics*, Academic Press, New York, 1982.

Goldberg, R., E. Kopp, G. Witt, and W. Swartz, An overview of NLC-91: A rocket/radar study of the polar summer mesosphere, *Geophys. Res. Lett.*, *20*, 2443–2446, 1993.

Gumbel, J., Aerodynamic influences on atmospheric in situ measurements from sounding rockets, *J. Geophys. Res.*, *106*, 10,553–10,563, 2001.

Hesstvedt, E., Note on the nature of noctilucent clouds, *J. Geophys. Res.*, *66*, 1985–1987, 1961.

Hillert, W., F.-J. Lübken, and G. Lehmacher, TOTAL: A rocket-borne instrument for high resolution measurements of neutral air turbulence during DYANA, *J. Atmos. Terr. Phys.*, *56*, 1835–1852, 1994.

Hines, C. O., Tropopausal mountain waves over Arecibo: a case study, *J. Atmos. Sci.*, *46*, 476–488, 1989.

Hunten, D. M., R. P. Turco, and O. B. Toon, Smoke and dust particles of meteoric origin in the mesosphere and stratosphere, *J. Atmos. Sci.*, *37*, 1342–1357, 1980.

Jensen, E., and G. E. Thomas, A growth-sedimentation model of polar mesospheric clouds: Comparions with SME measurements, *J. Geophys. Res.*, *93*, 2461–2473, 1988.

Jensen, E., and G. E. Thomas, Numerical simulations of the effects of gravity waves on noctilucent clouds, *J. Geophys. Res.*, *99*, 3421–3430, 1994.

Jensen, E., G. E. Thomas, and O. B. Toon, On the diurnal variation of noctilucent clouds, *J. Geophys. Res.*, *94*, 14,693–14,702, 1989.

Jensen, E. J., A numerical model of polar mesospheric cloud formation and evolution, Ph.D. thesis, University of Colorado, 1989.

Jesse, O., Auffallende Erscheinungen am Abendhimmel, *Met. Zeit.*, *2*, 311–312, 1885.

Klostermeyer, J., A simple model of the ice particle size distribution in noctilucent clouds, *J. Geophys. Res.*, *103*, 28743–28752, 1998.

Klostermeyer, J., Effect of tidal variability on the mean diurnal variation of noctilucent clouds, *J. Geophys. Res.*, *106*, 9749–9755, 2001.

Körner, U., and G. Sonnemann, Global 3d-modelling of the water vapor concentration of the mesosphere/mesopause region and implications with respect to the nlc region, *J. Geophys. Res.*, *in print*, 2001.

Langer, M., K. Müller, and K. H. Fricke, Rayleigh lidar detection of aerosol echoes from noctilucent cloud altitudes at the Arctic circle, *Geophys. Res. Lett.*, *22*, 381–384, 1995a.

Langer, M., K. P. Müller, K. H. Fricke, K. Römke, and F.-J. Lübken, Application of the Rayleigh-lidar technique to observations of noctilucent clouds, in *Proceedings of the 12th ESA Symposium on European Rocket and Balloon Programmes and Related Research, Lillehammer, Norway (ESA SP)*, pp. 81–86, Eur. Space Agency, Neuilly, France, 1995b.

Lindzen, R. S., Turbulence and stress owing to gravity wave and tidal breakdown, *J. Geophys. Res.*, *86*, 9707–9714, 1981.

Lübken, F.-J., On the extraction of turbulent parameters from atmospheric density fluctuations, *J. Geophys. Res.*, *97*, 20,385–20,395, 1992.

Lübken, F.-J., Aerodynamical effects in number density measurements in the lower thermosphere with the CONE instrument, *Adv. Space Res.*, *19*(1), 139–144, 1997a.

Lübken, F.-J., Seasonal variation of turbulent energy dissipation rates at high latitudes as determined by insitu measurements of neutral density fluctuations, *J. Geophys. Res.*, *102*, 13,441–13,456, 1997b.

Lübken, F.-J., Thermal structure of the Arctic summer mesosphere, *J. Geophys. Res.*, *104*, 9135–9149, 1999.

Lübken, F.-J., U. von Zahn, E. V. Thrane, T. Blix, G. A. Kokin, and S. V. Pachomov, In situ measurements of turbulent energy dissipation rates and eddy diffusion coefficients during MAP/WINE, *J. Atmos. Terr. Phys.*, *49*, 763–776, 1987.

Lübken, F.-J., W. Hillert, G. Lehmacher, and U. von Zahn, Experiments revealing small impact of turbulence on the energy budget of the mesosphere and lower thermosphere, *J. Geophys. Res.*, *98*, 20,369–20,384, 1993.

Lübken, F.-J., K. H. Fricke, M. Langer, P. Hoffmann, W. Singer, B. Inhester, and G. Witt, Simultaneous measurements of noctilucent clouds, polar mesosphere summer echoes, and the temperature near the mesopause, in *Proceedings of the 12th ESA Symposium on European Rocket and Balloon Programmes and Related Research, Lillehammer, Norway (ESA SP)*, pp. 61–66, Eur. Space Agency, Neuilly, France, 1995.

Lübken, F.-J., K.-H. Fricke, and M. Langer, Noctilucent clouds and the thermal structure near the Arctic mesopause, *J. Geophys. Res.*, *101*, 9489–9508, 1996.

Lübken, F.-J., M. Rapp, T. Blix, and E. Thrane, Microphysical and turbulent measurements of the Schmidt number in the vicinity of polar mesosphere summer echoes, *Geophys. Res. Lett.*, *25*, 893–896, 1998.

McLandress, C., G. C. Shepherd, B. H. Solheim, M. D. Burrage, P. B. Hays, and W. R. Skinner, Combined mesosphere/thermosphere winds using WINDII and HRDI data from the Upper Atmosphere Research Satellite, *J. Geophys. Res.*, *101*, 10,441–10,453, 1996.

Meyer, W., Intercomparison of wind measurements performed with metrockets, in *Proceedings of the 7th ESA Symposium on European Rocket and Balloon Programmes and Related Research, Loen, Norway (ESA SP–229)*, pp. 55–60, Eur. Space Agency, Neuilly, France, 1985.

Nussbaumer, V., K.-H. Fricke, M. Langer, W. Singer, and U. von Zahn, First simultaneous and common-volume observations of NLC and PMSE by lidar and radar, *J. Geophys. Res.*, *101*, 19161–19167, 1996.

Philbrick, C., J. Barnett, R. Gerndt, D. Offermann, W. P. Jr., P. Schlyter, J. Schmidlin, and G. Witt, Temperature measurements during the CAMP program, *Adv. Space Res.*, *4, No.4*, 153–156, 1984.

Pumphrey, H. C., D. Rind, J. M. Russell, and J. E. Harries, A preliminary zonal mean climatology of water vapor in the stratosphere and mesosphere, *Adv. Space Res.*, *21*, 1417–1420, 1998.

Rapp, M., J. Gumbel, and F.-J. Lübken, Absolute density measurements in the middle atmosphere, *Ann. Geophys.*, *19*, 571–580, 2001.

Schmidlin, F. J., The inflatable sphere: A technique for the accurate measurement of middle atmosphere temperatures, *J. Geophys. Res.*, *96*, 22,673–22,682, 1991.

Seele, C., and P. Hartogh, Water vapor of the polar middle atmsophere: annual variation and summer mesophere conditions as observed by ground-based microwave spectroscopy, *Geophys. Res. Lett.*, *26*, 1517–1520, 1999.

Stevens, M. H., C. R. Englert, M. E.Summers, and M. Rapp, MAHRSI observations of small scale variability in OH density and PMC brightness: modelling the distribution of water vapor at PMCs, *Eos. Trans. AGU*, *82*, 287, 2001.

Thomas, G. E., Mesopheric clouds and the physics of the mesopause region, *Rev. Geophys*, *29*, 553–575, 1991.

Thomas, G. E., Climatology of polar mesospheric clouds: interannual variability and implications for long term trends, in *Geophysical Monograph 87*, pp. 185–200, The upper mesosphere and lower thermosphere: a review of experiment and theory, 1995.

Thomas, G. E., and J. Olivero, Noctilucent clouds as possible indicators of global change in the mesosphere, *Adv. Space Res.*, *in print*, 2001.

Thomas, G. E., J. J. Olivero, E. J. Jensen, W. Schröder, and O. B. Toon, Relation between increasing methane and the presence of ice clouds at the mesopause, *Nature*, *338*, 490–492, 1989.

Toon, O. B., R. P. Turco, D. Westphal, R. Malone, and M. S. Liu, A multidimensional model for aerosols: description and computational analogs, *J. Atmos. Sci.*, *45*, 2123–2143, 1988.

Turco, R. P., O. B. Toon, R. C. Whitten, R. G. Keesee, and D. Hollenbach, Noctilucent clouds: Simulation studies of their genesis, properties and global influences, *Planet. Space Sci.*, *3*, 1147–1181, 1982.

Vincent, R. A., S. J. Allen, and S. D. Eckermann, *Gravity wave parameters in the lower stratosphere*, pp. 7–25, in: Gravity wave processes: their parameterization in global climate models, NATO ASI Ser. I, 50, edited by K. Hamilton, 1996.

Wälchli, U., J. Stegman, G. Witt, J. Y. N. Cho, C. A. Miller, M. C. Kelley, and W. E. Swartz, First height comparison of noctilucent clouds and simultaneous pmse, *Geophys. Res. Lett.*, *20*, 2845–2848, 1993.

Widdel, H. U., Foil chaff clouds as a tool for in-situ measurements of atmospheric motions in the middle atmosphere: their flight behaviour and implications for radar tracking, *J. Atmos. Terr. Phys.*, *52*, 89–101, 1990.

Wilhelm, N., and G. Witt, The SLIPS, a scattered light intensity profile sensor for rocket-borne investigations of noctilucent clouds, in *Workshop on noctilucent clouds*, p. 69, Valgus, Tallinn, Estonia, 1989.

Witt, G., Height, structure and displacements of noctilucent clouds, *Tellus XIV*, *1*, 1–18, 1962.

Wu, Y., and H. U. Widdel, Observational evidence of a saturated gravity wave spectrum in the mesosphere, *J. Atmos. Terr. Phys.*, *51*, 991–996, 1989.

Figure 1. Seven temperature profiles derived from absolute density measurements with the ionization gauges TOTAL and CONE. Subsequent profiles have been shifted by 30 K such that the actual temperature axis is only valid for the first profile of flight SCT03. For comparison we have overlayed each profile with a mean profile for August 1 taken from a compilation of falling sphere measurements by *Lübken* [1999].

Figure 2. All TOTAL and CONE temperature profiles measured in the summer polar mesopause region. The thick solid line shows the mean profile of the ionization gauge measurements. To the left of the profiles we have indicated the corresponding rms-variation every five kilometers.

Figure 3. Left panel: Comparison of the CONE temperature profile (thick dashed line) and noctilucent cloud altitude of flight SCT03 during the SCALE campaign in July 1993. In addition two falling sphere temperature profiles are shown which have been launched shortly before and after the sounding rocket flight. The hatched profile at the left ordinate (with the top abscissa being the corresponding x-axis) shows the lidar backscatter ratios R obtained during the rocket flights together with the statistical noise signal. The thick horizontal line designated 'SLIPS' indicates the maximum NLC signal detected onboard the sounding rocket by a broadband photometer [*Lübken et al.*, 1995]. The thin dashed line indicates the reference temperature profile from *Fleming et al.* [1990] for the month August and the latitude of Andøya. Right panel: Same as left panel but for flight ECT07 during the ECHO campaign in 1994.

Figure 4. Temperature profile measured with the TOTAL sensor during flight NAT13 (solid line) in comparison to the mean falling sphere profile from *Lübken* [1999] (thin dashed line). The NLC altitude as detected during flight NAD14 (launched 15 s after NAT13) is indicated with thick dashed horizontal lines [*Wälchli et al.*, 1993].

Figure 5. Left panel: Profiles of the zonal and meridional wind u and v (thick black and grey line) measured during flight SCS04 together with an estimate of the background winds indicated by the dotted lines, respectively. Right panel: hodograph of the wind fluctuations during flight SCS04 between 75 and 82 km. The grey ellipse shows the best fit to the data. The dotted line indicates the background wind vector at 82 km altitude.

Figure 6. Temperature profiles measured during the CAMP campaign in 1982 at Esrange. 900 m below the lowermost temperature minimum at 83.5 km a rocket borne photometer of the Meteorological institute of Stockholm University detected a NLC. This Figure has been reproduced from *Philbrick et al.* [1984], copyright by COSPAR.

Figure 7. Time-altitude dependence of temperature, ice mass, water vapor mixing ratio, saturation ratio, total ice number density and mean ice radius during the formation and growth of a noctilucent cloud. The black isolines overlayed on each plot show lines of constant backscatter ratio as it would be observed by a lidar with a laser wavelength of 532 nm.

Figure 8. Results of trajectory simulations for 40 test particles initially equally distributed between 84 and 90 km altitude. Chart a shows the trajectories on top of the vertical wind field. Chart b presents the radii along the particle trajectories. In Chart c we show the scattering signature of the particles as a function of altitude and time, and in Chart d the scattering signature is shown along the particle trajectories. The thick solid line in Chart c indicates the line with S=1.

Figure 9. Temperature wave amplitudes used in the model calculations (black line) compared to actually measured temperature disturbances during flight SCT03 (grey line).

Figure 10. Same as Figure 7 but for the presence of a gravity wave with a period of 470 min, a horizontal wavelength of 595 km, and a vertical wavelength of 6 km.

Figure 11. Altitude versus horizontal distance variation of the temperature disturbance due to the gravity wave for different times. The black isolines show the backscatter ratio for a wavelength of 532 nm.

Figure 12. Same as Figure 11 but for a wave period of 60 min.

Figure 13. Same as for Figure 8 but for a wave with a period of 500 min.

Figure 14. DABR variation with time for different wave parameters compared to the reference case in the absence of a wave. For an explanation of the different line types see insert.

Table 1. Listing of all TOTAL and CONE flights. In the last column the gauge type is indicated: T: TOTAL, C: CONE

Flight	Campaign	Date	Time (UT)	apogee [km]	gauge
NBT05	NLC-91	01.08.91	01:40:00	131	T
NAT13		09.08.91	23:15:00	130	T
SCT03	SCALE	28.07.93	22:23:00	128	C
SCT06		31.07.93	01:46:00	127	C
ECT02	ECHO	28.07.94	22:39:00	124	C
ECT07		31.07.94	00:50:33	126	C
ECT12		12.08.94	00:53:00	129	C

Table 2. Altitudes and temperature values of the temperature minima as well as the dominant vertical wavelength observed between 82 and 96 km altitude in the polar summer mesosphere during all summer flights.

flight	z_1 [km]	T_1 [K]	z_2 [km]	T_2 [K]	z_3 [km]	T_3 [K]	λ_z [km]
SCT03	83.4	136.0	88.8	128.9	93.4	128.3	6.0
SCT06	85.8	110.3	89.8	142.2	92.4	141.6	5.5
ECT02	87.4	113.2	90.3	140.5	96.0	154.8	5.0
ECT07	83.3	127.7	87.6	134.0	90.0	138.5	7.6
ECT12	85.7	128.2	88.0	139.5	91.8	154.1	5.6
NAT13	84.7	144.5	86.1	136.7	91.5	141.8	6.8
NBT05	86.4	140.0			92.8	139.6	8.0

Table 3. Gravity wave parameters derived from falling sphere and chaff flights launched close in time to the sounding rocket launches listed in Table 1. Hodographs have been determined in an altitude range between ~ 70 and 80 km. In cases where an unambigous ellipse couldn't be identified in the hodograph, no gravity wave parameters were determined. dv_T/dz denotes the wind shear of the background horizontal wind transverse to the direction of phase propagation, R is the axial ratio of the polarization ellipse, T is the wave period, and λ_x the horizontal wavelength of the wave.

Flight	Date	Time UT	dv_T/dz [m/s/km]	R	T [min]	λ_x [km]
NBS01	01/08/91	01:03:00	0.27	0.67	501	883
NBS06	01/08/91	01:54:00	1.00	0.68	470	790
NBC07	01/08/91	02:24:00	0.00	0.50	383	590
NAS12	09/08/91	22:53:00	–	–	–	–
NAS18	10/08/91	00:06:00	–	–	–	–
NAC19	10/08/91	00:24:00	0.00	0.72	551	900
SCS02	23/07/93	22:07:00	–	–	–	–
SCS04	23/07/93	22:28:00	1.50	0.70	470	595
SCS07	01/08/93	02:06:00	2.00	0.40	218	227
ECS03	28/07/94	23:03:00	2.50	0.10	33	27
ECS06	31/07/94	00:27:00	1.00	0.78	553	1013
ECS08	31/07/94	01:09:20	1.00	0.75	530	931
ECS13	12/08/94	01:14:00	–	–	–	–

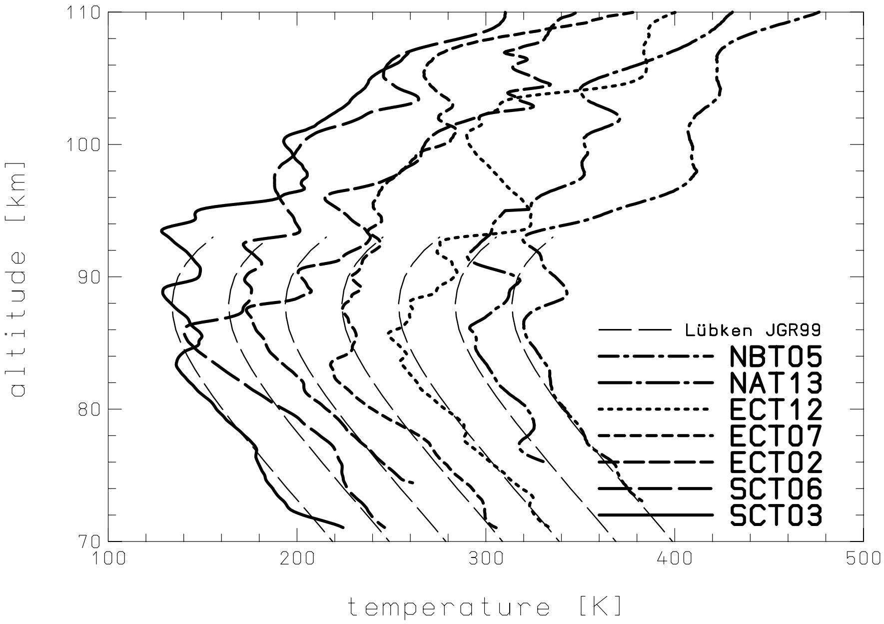

110
100
90
80
70
altitude [km]
100
200
300
400
500
temperature [K]
Lübken JGR99
NBT05
NAT13
ECT12
ECT07
ECT02
SCT06
SCT03

Figure 1

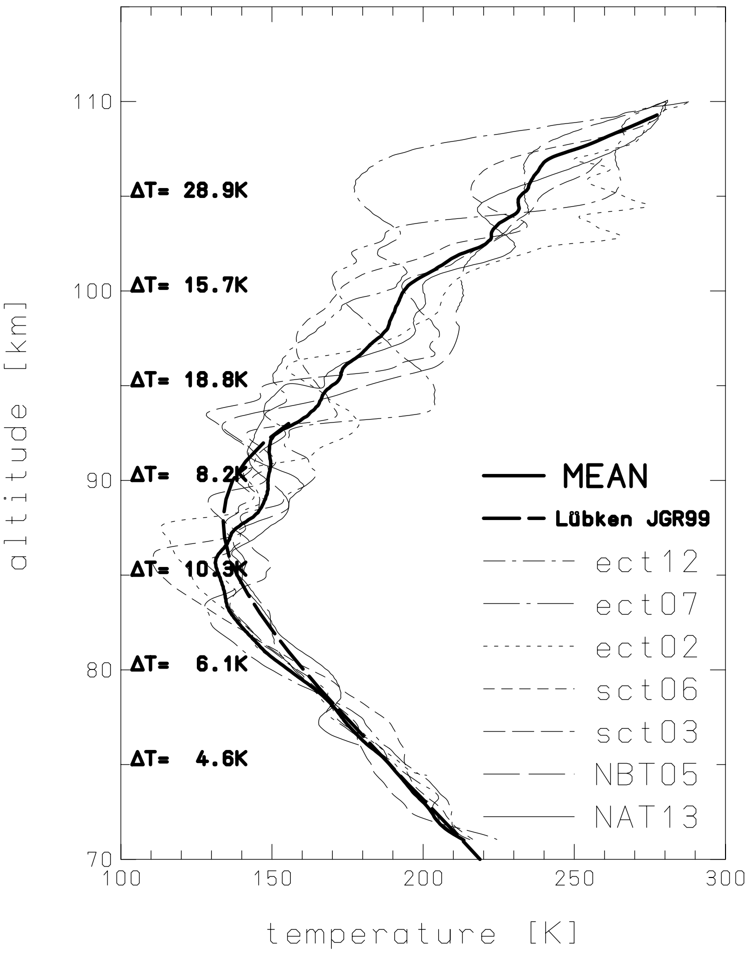

ΔT= 28.9K
ΔT= 15.7K
ΔT= 18.8K
ΔT= 8.2K
ΔT= 10.3K
ΔT= 6.1K
ΔT= 4.6K
MEAN
Lübken JGR99
ect12
ect07
ect02
sct06
sct03
NBT05
NAT13
110
100
90
80
70
100
150
200
250
300
altitude [km]
temperature [K]

Figure 2

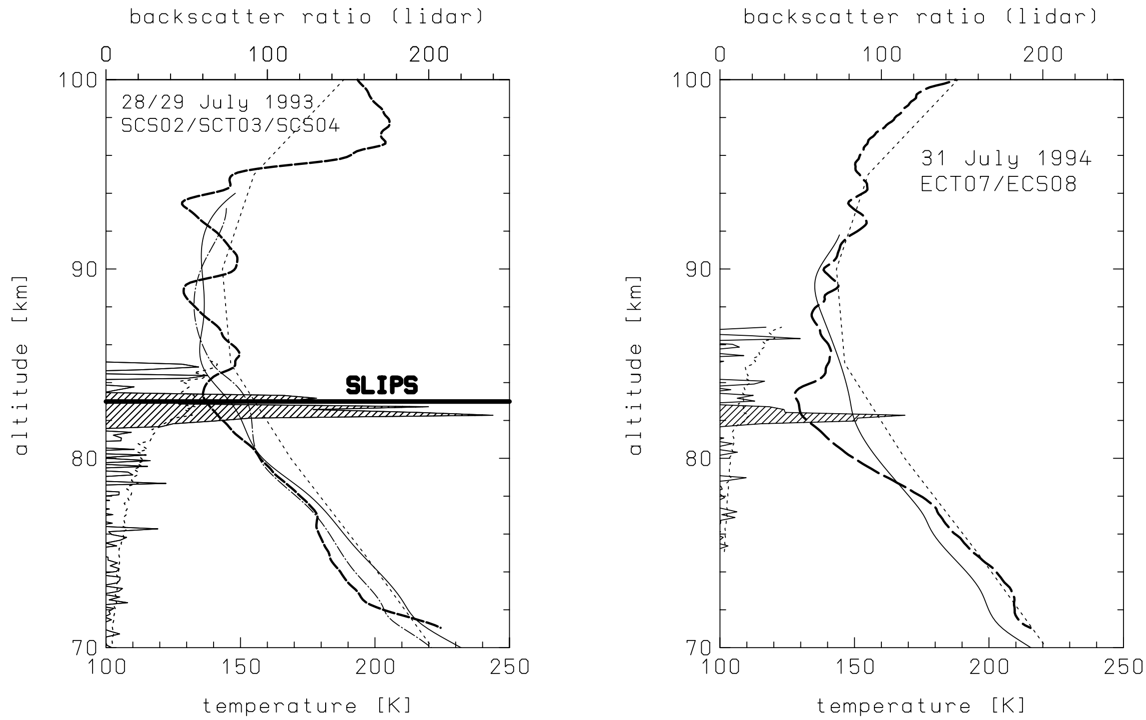
backscatter ratio (lidar)
0
100
200
100
90
80
70
28/29 July 1993
SCS02/SCT03/SCS04
SLIPS
altitude [km]
100
150
200
250
temperature [K]
backscatter ratio (lidar)
0
100
200
100
90
80
70
31 July 1994
ECT07/ECS08
altitude [km]
100
150
200
250
temperature [K]

Figure 3

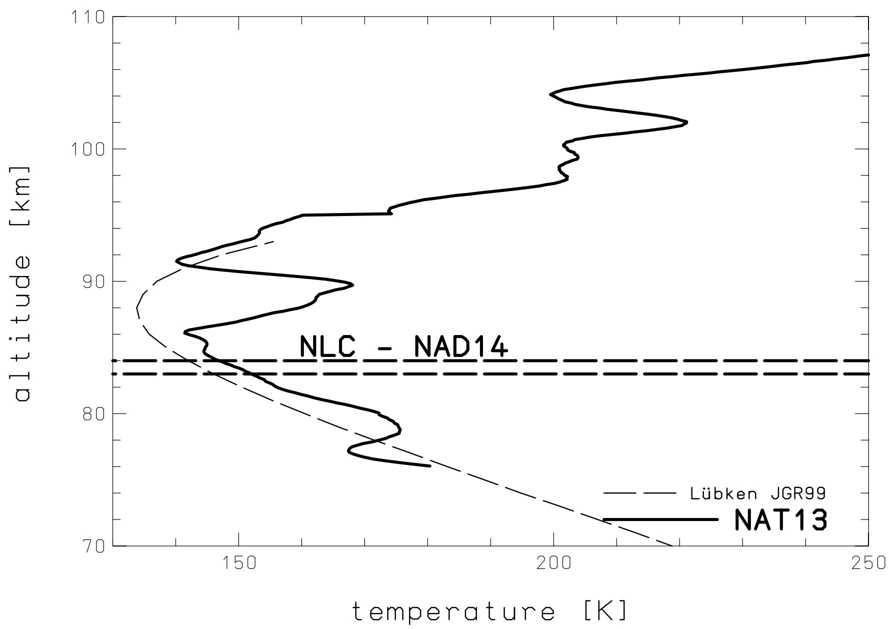
110
100
90
80
70
150
200
250
altitude [km]
temperature [K]
NLC - NAD14
Lübken JGR99
NAT13

Figure 4

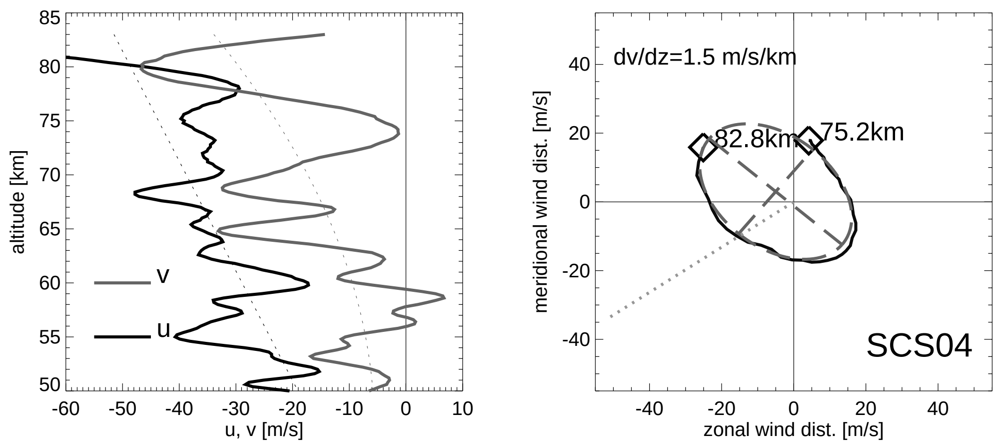

altitude [km]
u, v [m/s]
v
u
meridional wind dist. [m/s]
zonal wind dist. [m/s]
dv/dz=1.5 m/s/km
82.8km
75.2km
SCS04

Figure 5

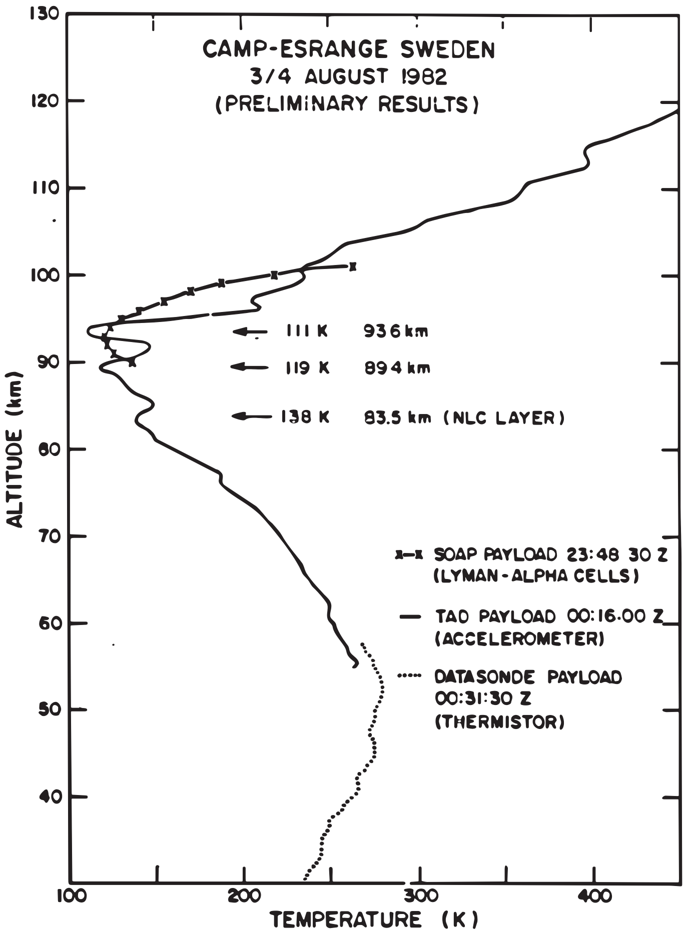

CAMP-ESRANGE SWEDEN
3/4 AUGUST 1982
(PRELIMINARY RESULTS)
111 K 93.6 km
119 K 89.4 km
138 K 83.5 km (NLC LAYER)
SOAP PAYLOAD 23:48 30 Z
(LYMAN-ALPHA CELLS)
TAD PAYLOAD 00:16.00 Z
(ACCELEROMETER)
DATASONDE PAYLOAD
00:31:30 Z
(THERMISTOR)
ALTITUDE (km)
TEMPERATURE (K)
130
120
110
100
90
80
70
60
50
40
100
200
300
400

Figure 6

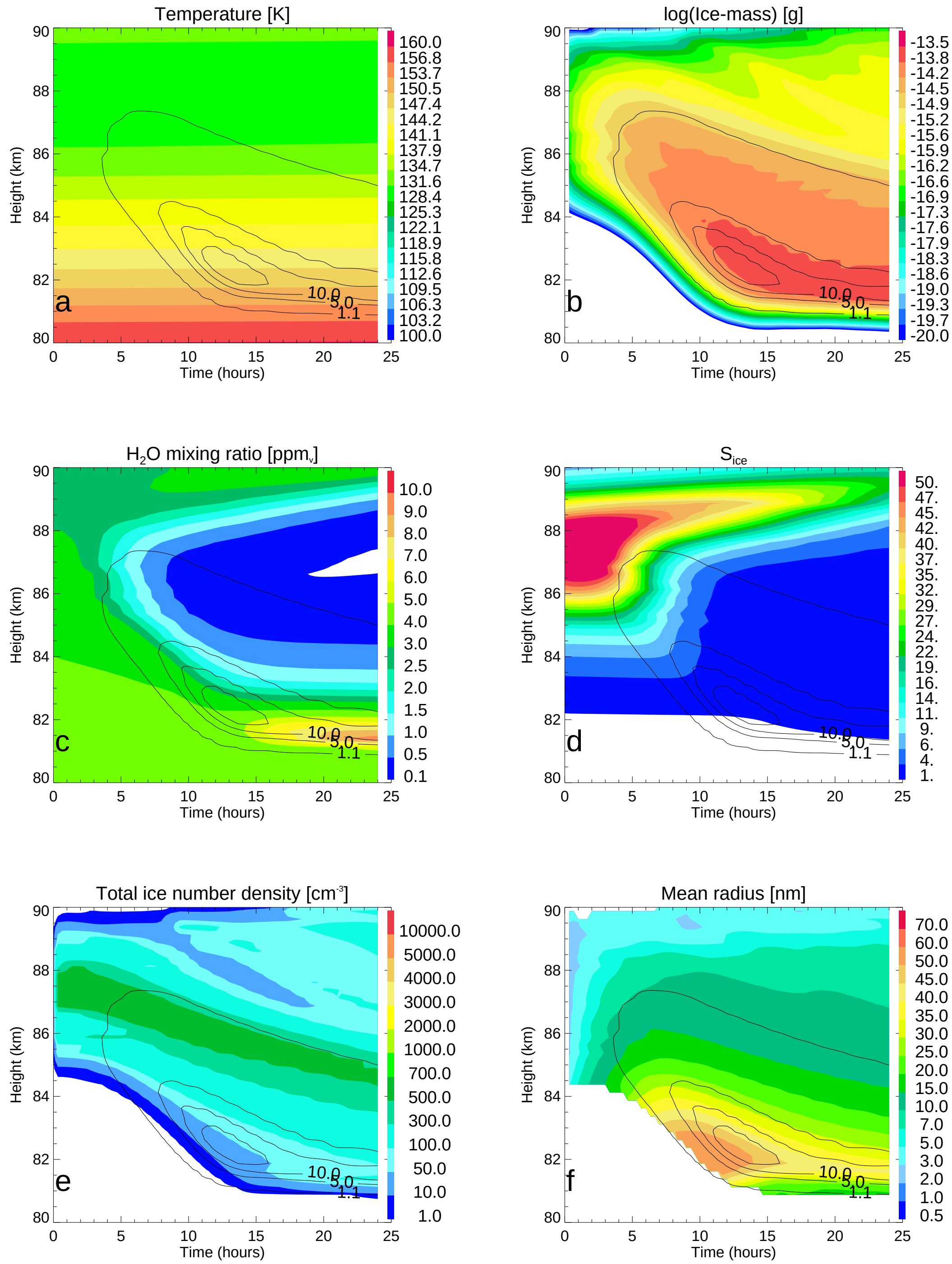

Temperature [K]
log(Ice-mass) [g]
H2O mixing ratio [ppmv]
Sice
Total ice number density [cm-3]
Mean radius [nm]
Height (km)
Time (hours)
a
b
c
d
e
f
10.0
5.0
1.1

Figure 7

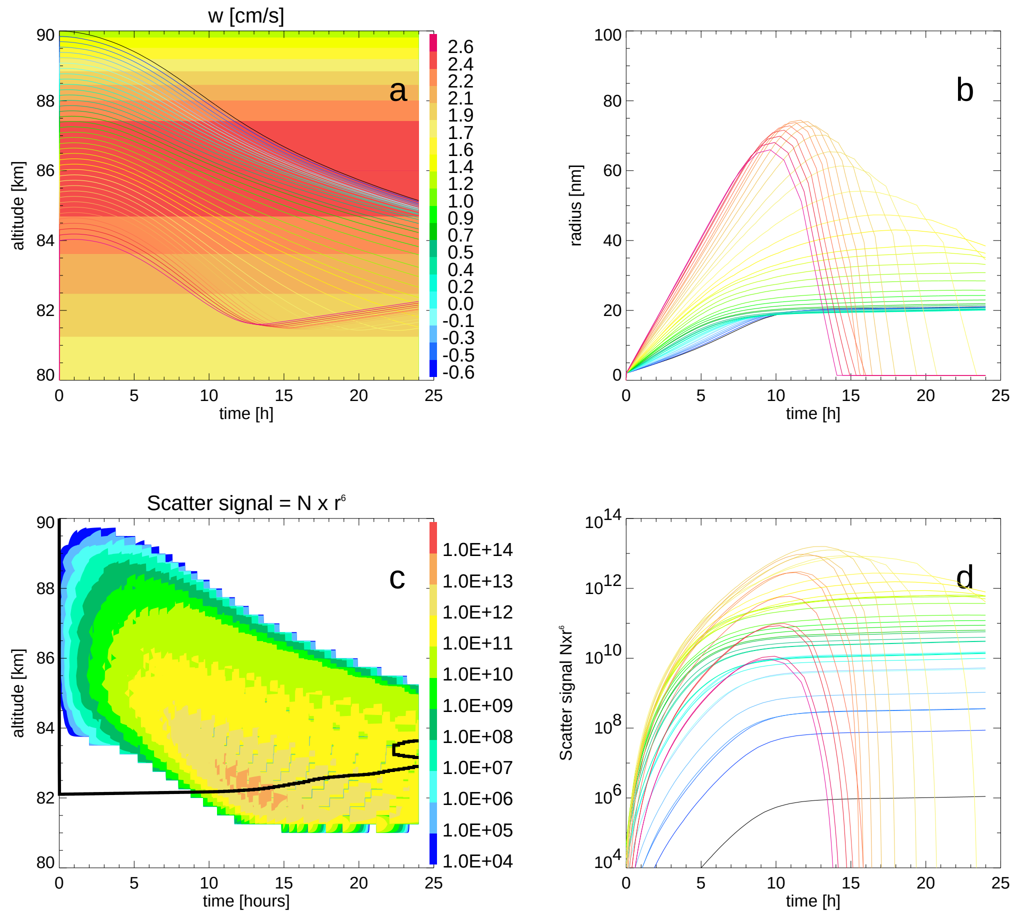
w [cm/s]
a
altitude [km]
time [h]
b
radius [nm]
time [h]
Scatter signal = N x r⁶
c
altitude [km]
time [hours]
d
Scatter signal Nxr⁶
time [h]

Figure 8

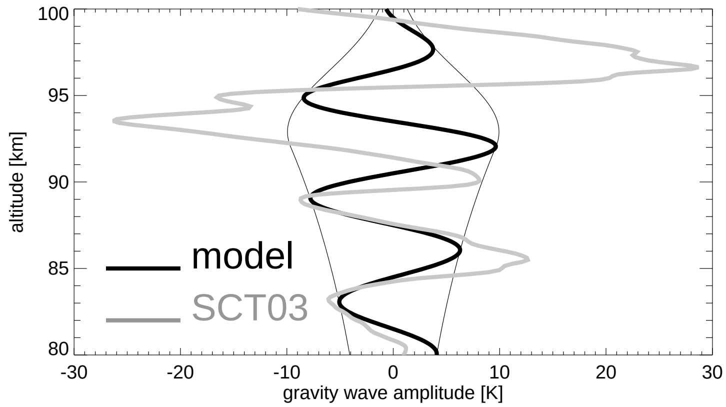

100
95
90
85
80
altitude [km]
-30
-20
-10
0
10
20
30
gravity wave amplitude [K]
model
SCT03

Figure 9

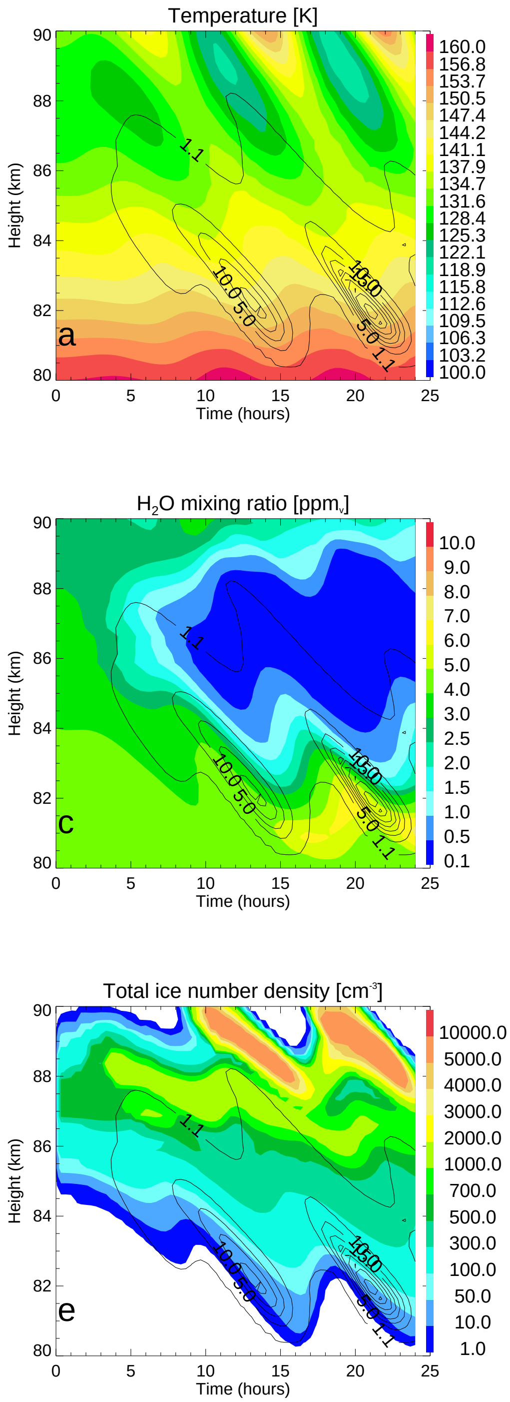
Temperature [K]
160.0 156.8 153.7 150.5 147.4 144.2 141.1 137.9 134.7 131.6 128.4 125.3 122.1 118.9 115.8 112.6 109.5 106.3 103.2 100.0
a
log(Ice-mass) [g]
-13.5 -13.8 -14.2 -14.5 -14.9 -15.2 -15.6 -15.9 -16.2 -16.6 -16.9 -17.3 -17.6 -17.9 -18.3 -18.6 -19.0 -19.3 -19.7 -20.0
b
H2O mixing ratio [ppmv]
10.0 9.0 8.0 7.0 6.0 5.0 4.0 3.0 2.5 2.0 1.5 1.0 0.5 0.1
c
Sice
50. 47. 45. 42. 40. 37. 35. 32. 29. 27. 24. 22. 19. 16. 14. 11. 9. 6. 4. 1.
d
Total ice number density [cm-3]
10000.0 5000.0 4000.0 3000.0 2000.0 1000.0 700.0 500.0 300.0 100.0 50.0 10.0 1.0
e
Mean radius [nm]
70.0 60.0 50.0 45.0 40.0 35.0 30.0 25.0 20.0 15.0 10.0 7.0 5.0 3.0 2.0 1.0 0.5
f
Height (km)
Time (hours)

Figure 10

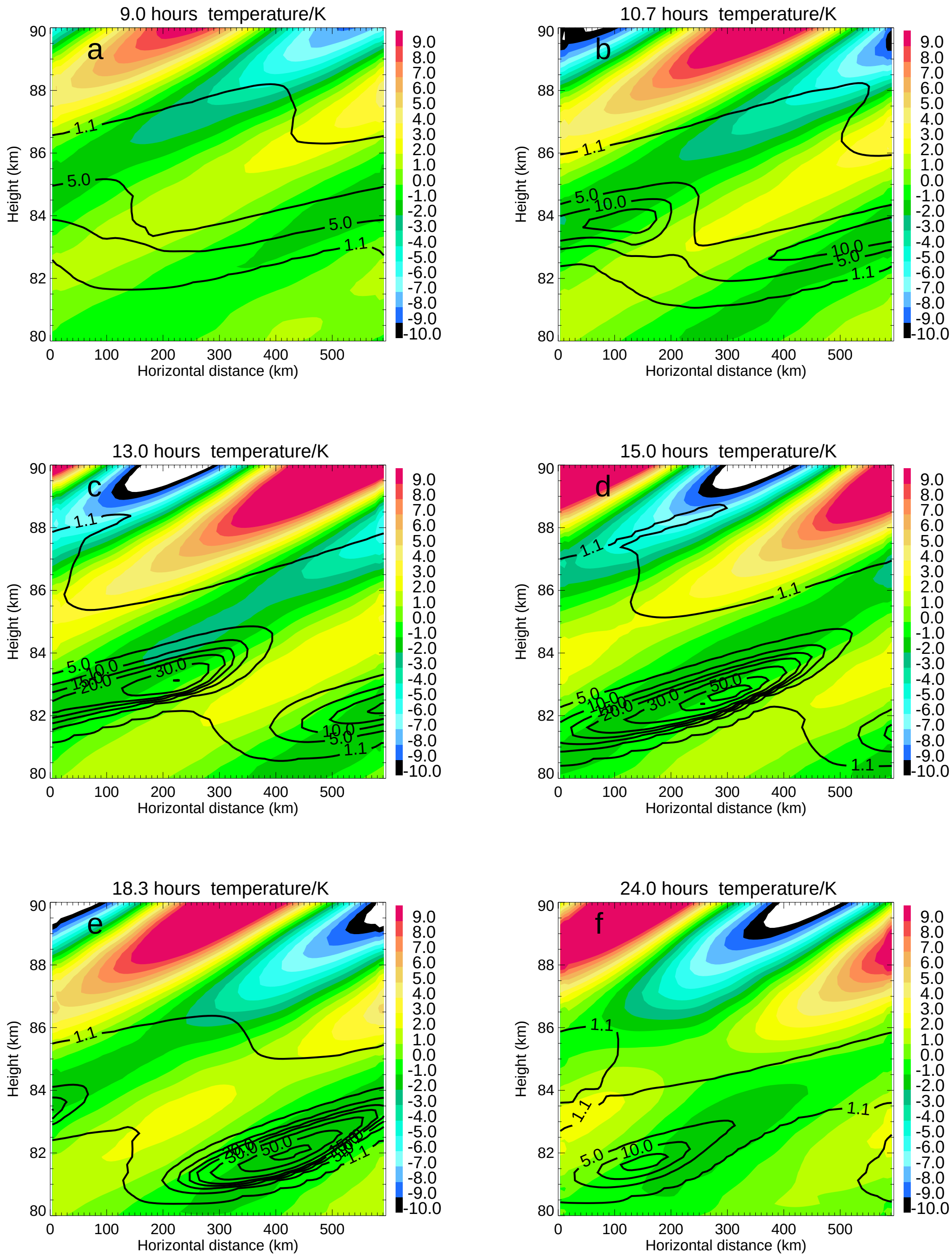
9.0 hours temperature/K
10.7 hours temperature/K
13.0 hours temperature/K
15.0 hours temperature/K
18.3 hours temperature/K
24.0 hours temperature/K
a
b
c
d
e
f
Height (km)
Horizontal distance (km)
9.0
8.0
7.0
6.0
5.0
4.0
3.0
2.0
1.0
0.0
-1.0
-2.0
-3.0
-4.0
-5.0
-6.0
-7.0
-8.0
-9.0
-10.0

Figure 11

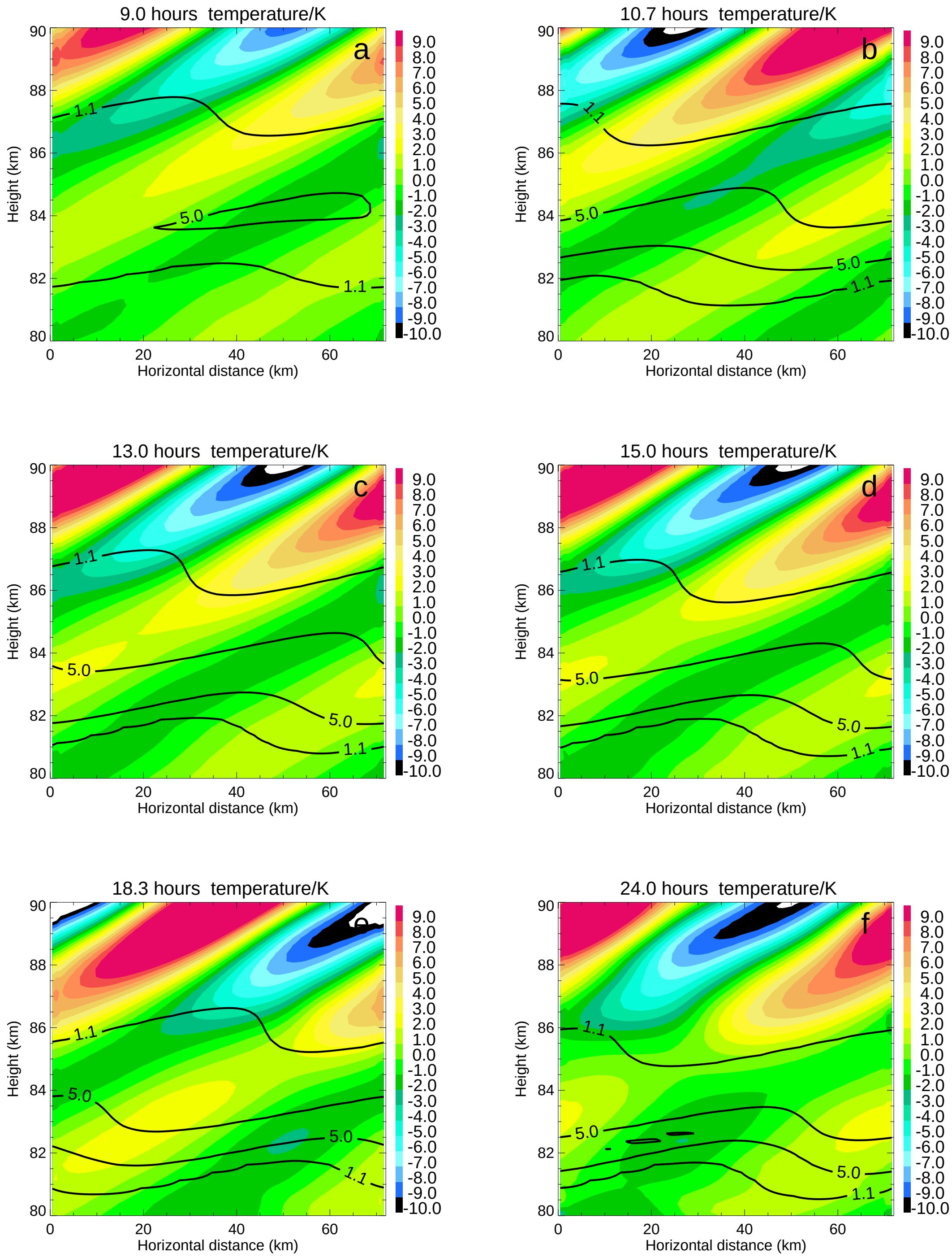
9.0 hours temperature/K
a
10.7 hours temperature/K
b
13.0 hours temperature/K
c
15.0 hours temperature/K
d
18.3 hours temperature/K
e
24.0 hours temperature/K
f
Height (km)
Horizontal distance (km)
9.0
8.0
7.0
6.0
5.0
4.0
3.0
2.0
1.0
0.0
-1.0
-2.0
-3.0
-4.0
-5.0
-6.0
-7.0
-8.0
-9.0
-10.0
1.1
5.0

Figure 12

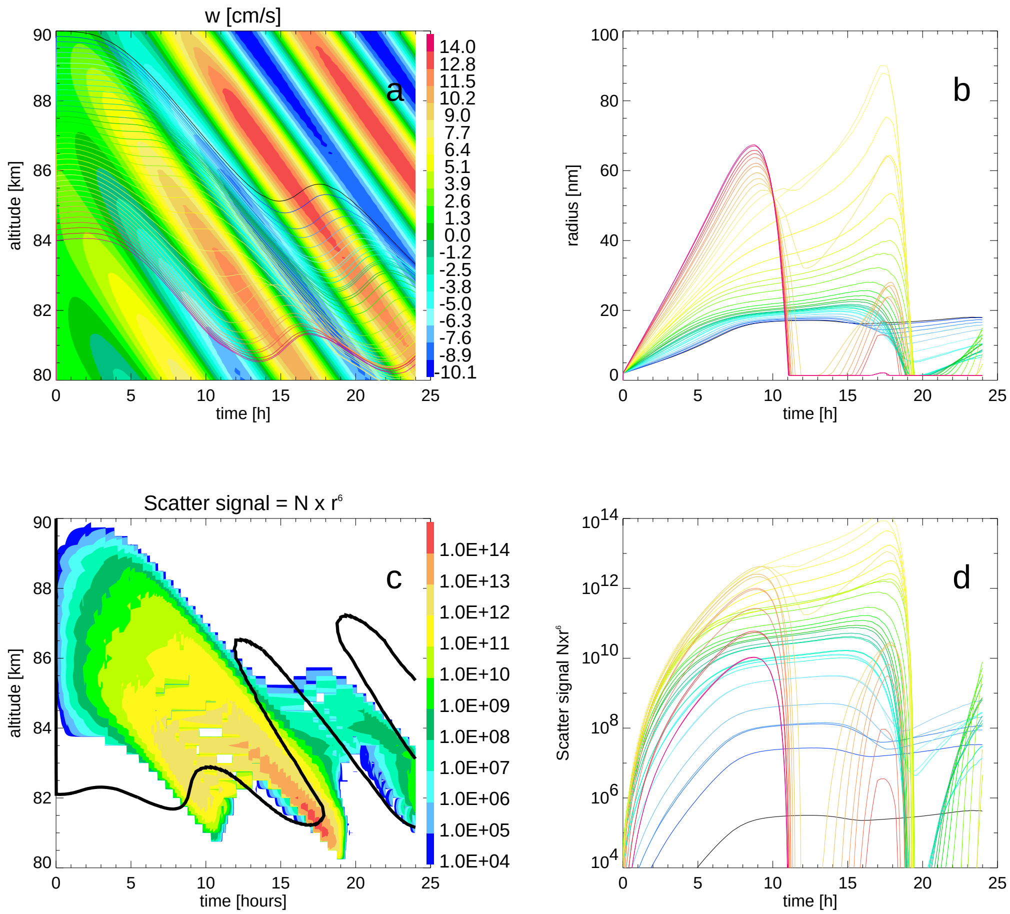
w [cm/s]
a
altitude [km]
time [h]
14.0
12.8
11.5
10.2
9.0
7.7
6.4
5.1
3.9
2.6
1.3
0.0
-1.2
-2.5
-3.8
-5.0
-6.3
-7.6
-8.9
-10.1
b
radius [nm]
time [h]
Scatter signal = N x r⁶
c
altitude [km]
time [hours]
1.0E+14
1.0E+13
1.0E+12
1.0E+11
1.0E+10
1.0E+09
1.0E+08
1.0E+07
1.0E+06
1.0E+05
1.0E+04
d
Scatter signal Nxr⁶
time [h]

Figure 13

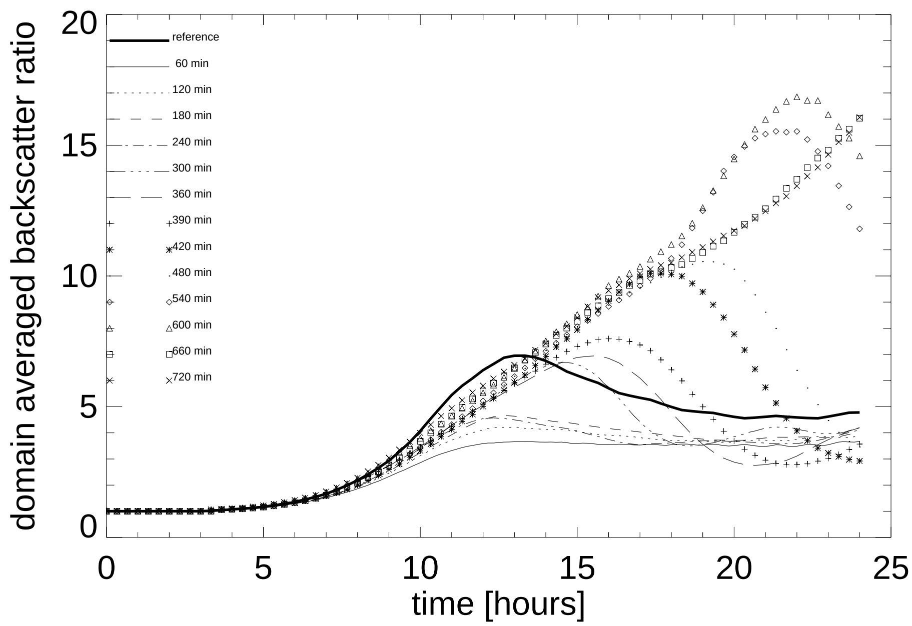
domain averaged backscatter ratio
time [hours]
reference
60 min
120 min
180 min
240 min
300 min
360 min
390 min
420 min
480 min
540 min
600 min
660 min
720 min
0
5
10
15
20
25

Figure 14